Cryo-EM structure and regulation of human NAD kinase

Prakash P Praharaj, Yang Li, Charline Mary, Mona H Soflaee, Kevin Ryu, Dohun Kim, Diem Tran, Trishna Dey, Harrison Tom, Halie Rion, et al.

Cryo-EM structure and regulation of human NAD kinase

Prakash P. Praharaj[1,†], Yang Li[2,†], Charline Mary[3,†], Mona H. Soflaee[1], Kevin Ryu[1], Dohun Kim[1], Diem Tran[1], Trishna Dey[1], Harrison Tom[1], Halie Rion[1], , Muriel Gelin[3], Andrew Lemoff[4], Lauren G. Zacharias[1], João S. Patricio[1], Thomas P. Mathews[1], Zhe Chen[2], Corinne Lionne[3], Gerta Hoxhaj[1,*], Gilles Labesse[3,*]

Affiliations:

[1]Children's Medical Center Research Institute, University of Texas Southwestern Medical Center, 5323 Harry Hines Boulevard, Dallas, TX 75390, USA.

[2]Department of Biophysics, University of Texas Southwestern Medical Center, Dallas, TX 75390, USA.

[3]Atelier de Biologie Chimie Informatique Structurale, Centre de Biologie Structurale, Univ Montpellier, CNRS, INSERM, 29 rue de Navacelles, 34090 Montpellier, France.

[4]Department of Biochemistry, University of Texas Southwestern Medical Center, Dallas, TX 75390, USA.

*Correspondence to senior authors GL and GH

Email: labesse@cbs.cnrs.fr; gerta.hoxhaj@utsouthwestern.edu.

[†]These authors contributed equally to this work.

Abstract

Reduced nicotinamide adenine dinucleotide phosphate (NADPH) is a crucial reducing cofactor for reductive biosynthesis and protection from oxidative stress. To fulfill their heightened anabolic and reductive power demands, cancer cells must boost their NADPH production. Pro-growth and mitogenic protein kinases promote the activity of cytosolic NAD kinase (NADK), which produces $NADP^+$, a limiting NADPH precursor. However, the molecular architecture and mechanistic regulation of human NADK remain undescribed. Here, we report the cryo-EM structure of human NADK, both in its apo-form and in complex with its substrate NAD^+, revealing a tetrameric organization with distinct structural features. We discover that the N-terminal and C-terminal tails of NADK have opposing effects on its enzymatic activity and cellular NADP(H) levels. Specifically, the C-terminal region is critical for NADK activity, whereas the N-terminal region exhibits an inhibitory role. This study reveals new molecular insights into the regulation of a vital enzyme governing NADP(H) production.

Keywords: Reducing power, NADP, cryo-EM, NADK, enzyme regulation.

Teaser

The cryo-EM structure of human NADK in its free form and in complex with NAD^+ reveals new insights into its regulation.

INTRODUCTION

Reduced nicotinamide adenine dinucleotide phosphate (NADPH) serves as a vital reducing cofactor for anabolic biosynthetic pathways, including lipid, nucleotide, and amino acid synthesis (*1, 2*). Additionally, NADPH fuels antioxidant systems, protecting cells from the reactive oxygen species (ROS) (*3*). Cancer cells enhance NADPH production to meet their increased anabolic and reductive power demands (*4, 5*). Cells maintain NADPH pools in different subcellular compartments, such as the cytosol and mitochondria. NADPH levels are regulated by NAD kinases, specifically cytosolic NADK and mitochondrial NADK2, which catalyze the synthesis of $NADP^+$, the limiting precursor for NADPH production, within their respective locations (*6-9*). However, until recently, we had a limited understanding of the regulation of NADPH biosynthesis.

At the molecular level, several protein kinases, including Akt, PKC, and ERK, have been shown to phosphorylate NADK at conserved serine residues within the N-terminal regulatory domain (*10-13*). These phosphorylation events stimulate NADK activity, increasing the cellular NADPH pool to support cancer cell growth. Emerging evidence suggests that NADK is a promising therapeutic target in cancer (*14*). Activating mutations of NADK have been observed in pancreatic cancer (*15*), while suppression of its activity hinders tumor growth in various cancers, including pancreatic cancer. Furthermore, NADK activity has been implicated in promoting breast cancer metastasis (*16*) and lymph node metastasis of lung cancer (*17*), highlighting the crucial role of NADK-dependent NADPH synthesis in cancer growth and spread. To elucidate the impact of cancer mutations and enable precise therapeutic targeting, detailed structural information on human NADK (hsNADK) is necessary.

In this study, we report the cryo-EM structure of hsNADK, both in its free form and bound to its substrate NAD^+. In contrast to human mitochondrial NADK2 (*18, 19*), hsNADK, akin to its counterparts in most species, including bacteria and yeast, exists as a tetramer. Animal cytosolic NAD kinases, including hsNADK, possess unique extensions that may regulate the conserved catalytic core (*7, 20*). Through biochemical and metabolic characterization of various deletion and point mutants, we highlight the significance of critical structural elements, including the N-terminal and C-terminal disordered extensions, in hsNADK cellular function.

RESULTS

Cryo-EM structure of full-length hsNADK reveals tetrameric organization primed for catalysis

We solved the cryo-EM structure of full-length human NADK ($NADK_{FL}$) at an overall resolution of 3.2 Å with D2 symmetry (**Figs. 1A and 1B**). $NADK_{FL}$ with a C-terminal FLAG tag was purified from HEK293 cells, and was frozen on the grid prior to imaging with an electron microscope. The cryo-EM structure revealed a well-organized tetramer, similar to its bacterial and yeast counterparts but distinct from the dimeric human mitochondrial NADK2. Each $NADK_{FL}$ monomer comprises of an N-terminal domain (residues 96-237) and a C-terminal domain (residues 238-430), both of which are well conserved (**Figs. 1C, S1A, S1B, and S2A**). The C-terminal domain includes a conserved helix at its distal end (residues 413-424), positioned between the two domains, with its C-terminal end oriented toward the active site. The active site is built similarly to other NADKs and located at the interface between the N-terminal domain from one monomer and the C-terminal domain from a second monomer (*21, 22*) (**Fig. 1C**).

The cryo-EM structure resembles the crystal structure of a truncated human NADK form (residues 68-426), which lacks most of the N- and C-terminal regions (deposited in the Protein Data Bank, 3PFN, not yet published). Both structures aligned well, particularly in the catalytic core, with RMSD reaching 2.1 Å for the whole tetramer and ranging from 1.0 to 1.5 Å at the monomer level (**Figs. 1D and S2B**). While the lack of extra density prevented us from modeling part of the highly flexible N- and C-terminal extensions (residues 1-94 and 431-446), the cryo-EM structure allowed us to visualize four additional conserved residues at the end of the C-terminal domain (amino acids W427-R430) (**Fig. 1E**). This C-terminal tail appears to point to the active site of another monomer in the cryo-EM structure but is absent in the crystal structure 3PFN (**Fig. 1E**). On the contrary, a segment of the N-terminal extension (residues 72-94), which was not visible in our cryo-EM structure, is clearly resolved in the crystal structure 3PFN, where it appears to swap between two monomers (**Fig. 1F**). This region, comprised of two small β-strands (residues 72-74 and 77-80), folds back against the N-terminal domain of another monomer and aligns with a short extended region (residues 97-101) to form a small β-sheet (**Fig. 1F**). Upon folding, residues F74, G75, A78 and V80 from the N-terminal tail make hydrophobic contacts with residues 197-200, L236, and P404-P406 from the catalytic domain of a second monomer (**Fig. 1G**). These contacts, near two hinge pivots (V201 and S407) in the catalytic domain, likely stabilize the N-terminal domains in a resting conformation (**Fig. S2C)** in the crystalline state due to domain swapping (**Fig.**

S2D). Hence, upon folding against the catalytic domain, the N-tail could influence the catalytic core's flexibility and activity.

Other differences between these two structures arise from two hinge motions: one involving the N-terminal domain, and the other involving the C-terminal helix (residues 413-424), with rotations relative to the C-terminal domain by ~10° and ~20°, respectively (**Figs. 1D, 1E, S2B, and S2D**). Interestingly, their respective pivots (V201 and S407) are very close in space (~4.5 Å), suggesting that their movements are coordinated, possibly through tight contacts between the C-terminal helix and a short segment (residues 209-214) in the N-terminal domain (**Fig. S2C**). Noteworthy, within this segment, two highly conserved residues, F211 and L212, position their backbone nitrogens towards the catalytic aspartate (D184), which is oriented inward in the cryo-EM structure as it is in the liganded forms of bacterial (*21*) and yeast (*22*) NADKs (**Fig. S2C**). In contrast, D184 points outward to the solvent in the 3PFN crystal structure (**Figs. 1H and S2C**). Finally, a small seven-residue loop (residues 290-297) shifts (by up to ~5.7 Å at proline P292) outward the ligand binding pocket in the cryo-EM structure (**Fig. 1H**).

Together, all these changes seem to prime the active site for catalysis in the cryo-EM structure, while the crystal structure cannot readily accommodate NAD^+ or $NADP^+$.

Cryo-EM structure of engineered hsNADK in Apo- and NAD^+-bound forms illuminate the catalytic core

To better visualize the catalytic core, we aimed to solve the cryo-EM structure of hsNADK bound to its substrate NAD^+. Prior to obtaining the cryo-EM structure, we faced numerous challenges in freezing hsNADK on grids, as the proteins often formed aggregates (**Fig. 2A**). This aggregation was likely due to oligomerization facilitated by disulfide bridges involving surface cysteine residues.

To enhance the structural integrity of hsNADK for cryo-EM analysis, we developed a new construct that removes the exposed cysteines (except for C424, which points to the active site) and omits the first 67 residues and the last 9 residues from $NADK_{FL}$. We also introduced an eight amino acid deletion (residues 81-88) and two substitutions (H89E and I90T) within the N-terminal tail to prevent any domain swapping (shown in **Fig. 1F**), which may stabilize hsNADK in its inactive form. We named this construct "$NADK_{esv}$", which stands for engineered stable version (**Fig. 2B**). $NADK_{esv}$ displayed reduced thermostability compared to the full-length enzyme in its apo-form, but higher thermostability in the presence of $NADP^+$ (**Fig. S3A**). It also displayed reduced

activity compared to the full-length enzyme (**Fig. S3B**), possibly due to stronger inhibition by its product $NADP^+$. However, it showed a similar binding affinity to NAD^+, which was measured via Isothermal Titration Calorimetry (**Figs. S3C and S3D**). Nonetheless, it achieved a higher degree of homogeneity, as judged by mass photometry (**Fig. 2C**), and was successfully applied to cryo-EM grids, resulting in fewer high-molecular-mass assemblies.

We first solved the apo-form of this engineered hsNADK by cryo-EM at a 2.8 Å resolution. This structure was highly similar to the full-length wild-type with a RMSD of 0.6-0.7 Å at the monomer level and 0.9 Å at the tetramer level (**Fig. 2D**).

Subsequently, we resolved a high-resolution cryo-EM structure of the $NADK_{esv}$ in a complex with NAD^+ at a 2.34 Å resolution (**Fig. 2E**). The NAD^+ molecule is clearly visible in the electron density map (**Fig. S3E**). The new structure closely resembles the apo-form of the same construct (RMSD of 0.7-0.8 Å at the monomer level and 0.9 Å the tetramer level), showing only subtle changes in the orientation of the N-terminal domain, along with minor rearrangements within the active site (**Figs. 2F and 2G**). In agreement with the absence of significant structural reorganization beside the hinge motion, the proteolysis profiles of hsNADKs were nearly identical in the presence or absence of NAD^+ (**Figs. S4A and S4B**).

Analysis of the active site of hsNADK revealed similar features conserved in most known NADK structures. In both cryo-EM apo-forms of $NADK_{FL}$ and $NADK_{esv}$, the active site appears ready to accommodate its substrate NAD^+ (**Fig. 2G**). Notably, in the C-terminal domain, the side chain of tyrosine Y327 is held in place by a neighboring aspartate D314' (denotes a residue from another monomer), positioning it to readily accommodate a nicotinamide moiety upon a slight rotation of its phenol ring (**Fig. 2G**). D314' is also poised to form a hydrogen bond with the amide group of the nicotinamide moiety, whereas asparagine N284 and glutamate E285 are positioned to interact with the adenine and ribose moieties of NAD^+, respectively (**Fig. 2G**). Threonine T325 is also aligned to form a hydrogen bond with the N1 nitrogen atom of adenine, similar to other NADKs. In the N-terminal domain, the hydrophobic side chains of F211 and L212 are also arranged to accommodate the adenine moiety (**Fig. 2G**). Their backbone nitrogen atoms hold the catalytic aspartate D184 in place, ready to catalyze the phosphotransfer.

The interactions between the NAD^+ molecule and $NADK_{esv}$ protein closely resemble those observed in other tetrameric NADKs. These interactions are characterized by conserved hydrophobic contacts and hydrogen bond networks that recognize the adenosine and ribose-nicotinamide

parts of NAD^+, while there are no strong interactions with the diphosphate part of the NAD^+ molecule (**Fig. 2G**). The only significant difference in hsNADK compared to all other NADKs of known structures is the absence of a highly conserved serine in the active site. This is replaced by alanine A330, which cannot form a hydrogen bond with the amide group of the nicotinamide moiety (**Fig. 2H**). The cryo-EM structure suggests that the recognition of this amide group may instead involve the nearby side chain of H351' (**Fig. 2H**), which adopts a distinct orientation in the apo form compared to the NAD^+-bound form (**Figs. S3F and S3G**). Both residues A330 and H351, along with the other residues that point into the active site (noted above), are strictly conserved within the cytoplasmic NADKs from animals.

In the NADK-NAD^+ complex, we also observed an additional density in the N-terminal tail, spanning residues F74-V80, which shows similar hydrophobic contacts as in the 3PFN structure (**Fig. 2I**). Albeit the weak density, these residues appear connected to S95, indicating a lack of domain swapping, due to the deletion of residues 81-88. Comparison of domain-swapped apo-form and the NADK-NAD^+ complex further highlights structural rearrangements at the juncture between the folded catalytic domain and the N- and C-terminal tails, characteristic of animal cytosolic NADKs. These changes are likely linked to specific functional regulations.

The N-Terminal tail acts as an inhibitory regulator in hsNADK

The cryo-EM structure suggests significant flexibility in the N-terminal region of hsNADK. Specifically, the segment encompassing the first 68 amino acids appears unfolded in $NADK_{FL}$ (**Fig. 3A**). This observation aligns with Alpha-Fold (*23*) predictions and is consistent with the presence of many polar residues in this region.

Noteworthy, the N-terminal domain of hsNADK undergoes numerous post-translational modifications, including phosphorylation at S44, S46, S48, S50, and S64, among others (https://www.phosphositeplus.org) (*24*). Several protein kinases target this region to stimulate NADK activity and NADP(H) generation. Notably, Akt predominantly phosphorylates S44, followed by S46 (*10*), PKC targets both S46 and S64 (*11, 12*), while ERK1/2 has been recently reported to target S48 and S50 (*13*). Analyses of post-translational modifications on hsNADK purified from HEK-293 cells cultured in 10% serum confirmed that the N-terminal domain of NADK is extensively modified, including phosphorylation at S15, S46, S48, and S64, as well as arginine methylation (e.g., R39, R41, and R45) and lysine methylation and/or acetylation (K12, K57, K77) (**Table S1**). Notably, the proteolysis profiles of modified hsNADK from HEK293 cells and that from

bacteria (lacking PTMs) were quite similar, with only trypsin, which primarily targets basic residues, showing distinct differences between the two forms (**Figs. S4A and S4B**). Deletion of this modified N-terminal domain Δ1-87 showed significant stability of the catalytic core (**Figs. S4A and S4B**). Thermal shift assays on samples purified from HEK-293 or *E. coli* cells (**Fig. S5**) revealed slight changes in thermostability, with a 2.8 °C reduction observed in the absence of PTMs. These findings suggest that the N-terminal tail of hsNADK integrates multiple signals that can modulate its thermostability.

To assess the impact of different regions of the N-terminal extension on NADK activity, we generated several deletion (Δ) variants, including Δ1-37, Δ1-68, Δ1-87, and Δ81-90, a small loop within the N-terminal extension (**Fig. 3B**). After expressing and purifying these variants from HEK-293 cells, we evaluated their *in vitro* activities alongside a hyperactive naturally occurring variant of NADK (Isoform 3), which lacks most of this N-terminal region (*10*) (**Figs. 3B-D**).

Deletion of the 1-37 region (Δ1-37) or the 81-90 loop (Δ81-90) had no effect on NADK activity. On the contrary, deletions of the 1-68 (Δ1-68) and 1-87 (Δ1-87) regions, which encompass the heavily post-translationally modified area, resulted in significantly increased activity, comparable to isoform 3 (**Fig. 3E**), confirming an inhibitory role for the N-terminal tail.

Next, we examined the impact of these variants on $NADP^+$ generation in cells. We expressed these variants in NADK-deficient HEK-293 cells and performed a 2-hour pulse labeling with D4-nicotinamide to assess the newly synthesized NAD^+ (M+3) and $NADP^+$ (M+3) (*10, 25*) (**Figs. 3F, 3G and S6A**). Consistent with the *in vitro* data, Δ1-37 and Δ81-90 showed no appreciable differences from the wild-type in $NADP^+$ synthesis. In contrast, Δ1-68, Δ1-87, and Isoform 3 exhibited increased levels of newly synthesized $NADP^+$ (**Fig. 3H**) as well as total $NADP^+$ and NADPH pools, without significantly affecting NAD^+ abundance (**Fig. S6B**). These results indicate a critical inhibitory role for the N-terminal tail for NADP(H) generation.

C-Terminal Tail is Crucial for the Activity of hsNADK

The cryo-EM map of $NADK_{FL}$ purified from mammalian cells allowed us to visualize the C-terminal domain (W427-R430) (**Fig. 1E**). This C-terminal tail appears to be embedded in the active site, located between the N-terminal and C-terminal domains (**Fig. 4A**). Tryptophan W427 within the C-tail is buried at the interface of two C-terminal domains, in the three cryo-EM structures (**Fig. S7A**). This feature is also observed in crystal structures of NADKs (*22, 26*) from gram-negative bacteria (PDB2AN1, PDB7QVS, PDB4HAO) and the yeast mitochondrial enzyme POS5

(PDB3AFO). Of note, the side chain of W427 folds back against the very C-terminal helix (**Figs. 4B and S7A)** and makes contact with L421 and F418 from the very same monomer **(Fig. S7B**). Additionally, it interacts with hydrophobic side-chains F355' and I358' from a second monomer (**Fig. S7B**). This configuration is further stabilized by a hydrogen bond network involving asparagine N428 and polar residues, such as T309', T310' and S352' from a second monomer (**Fig. S7C**).

The orientation of the remaining C-terminal tail varies across NADK structures, as it points into the active site only in hsNADK and mitochondrial yeast POS5 (PDB 3AFO), while it extends outward in bacterial counterparts (**Fig. S7D**). Notably, in the NAD^+-bound form, the side chain of R430 points toward the adenosine ribose of NAD^+, positioning it well to assist in the entry of the transferred phosphate (**Fig. 4B and S7E**). The R430A mutation or deletion of the C-tail (Δ431-446) did not lead to significant changes to the proteolytic profile or thermostability compared to the wild-type construct, suggesting that it adopts a similar overall fold (**Figs. S4 and S5**).

We also observed a weak but continuous electron density in the full-length apo-form between the N- and C-terminal domains, which likely represents the highly flexible C-terminal tail, although it could not be accurately modeled due to insufficient electron density. This elongated conformation agrees with the model predicted by AlphaFold (**Fig. 4A**). Accordingly, we slightly re-oriented this segment to better fit the extra density to the AlphaFold model (**Fig. S7E**).

While the C-terminal end (residues 431-446) was barely visible in our cryo-EM structures, it contains two conserved positions, glutamine Q433 and (to a lesser extent) F436, whose side chains point toward the $NAD(P)^+$ binding groove in our AlphaFold/$NADK_{FL}$ hybrid model (**Fig. S7F**).

To test the function of the C-terminal domain, we generated point mutations in the conserved residues (W427G, R430A, and F436A) and truncated the last 16 amino acids from the C-tail (Δ430-446) (**Fig. 4C**). We expressed and purified these variants from HEK-293 cells (**Fig. 4D**) and tested their activity *in vitro* (**Fig. 4E**). Remarkably, all mutants exhibited a substantial reduction in NADK activity, with W427G and R430A showing almost no activity (**Fig. 4E**). Consistently expressing these C-terminal variants in NADK-deficient HEK-293 cells, alongside the wild type, resulted in a significant reduction in $NADP^+$ biosynthesis and NADPH generation (**Figs. 4G and S6**). Together, these findings highlight the critical role of the C-terminal domain in NADK activity, likely through its influence on the active site.

DISCUSSION

Here, we report the cryo-EM structures of functional human NADK variants, both in full-length and an engineered stable variant, in both apo and in complex with its substrate NAD^+, highlighting structural and functional features typical of most tetrameric NADKs. We also reveal unique aspects, such as the presence of functionally important extensions at the N- and C-termini (see schematic model of hsNADK regulation **(Fig. 5).**

Our findings that partial and complete deletions of the N-terminal disordered region (Δ1-68, Δ1-87, isoform 3) significantly enhance NADK's enzymatic activity *in vitro*, as well as $NADP^+$ biosynthesis and NADP(H) pools in cells, support a model in which the N-terminal domain of NADK exerts an autoinhibitory effect on its function **(Fig. 5)** (*10*). Notably, the N-terminal tail of human NADK undergoes extensive modifications, including multiple phosphorylation events mediated by various protein kinases such as Akt, PKC, and ERK (*10-13*). These modifications would fine-tune NADK activity, thereby calibrating cellular signaling with the metabolic state. Although we were unable to fully resolve this N-terminal tail, future studies focused on identifying NADK binding partners that could stabilize this region, are expected to illuminate the detailed mechanisms by which phosphorylation events enhance NADK activity.

By contrast, the C-terminal tail has an opposing effect to that of the N-terminal domain and is essential for NADK enzyme function and NADP(H) production. Our high-resolution structures reveal that part of the C-terminal tail is integrated into the catalytic core, with R430 directly oriented towards the active site. This alignment provides insight into how mutations within the C-terminal domain can abrogate NADK function. It is likely that the C-terminal tail's proximity to the active site affects either NAD^+ binding or the phosphotransfer process.

Comparative analysis of NADK structures in inactive (3PFN) and active ($NADK_{FL}$) states suggests a model in which the N-terminal tails intertwine to lock the catalytic domains in an inactive conformation, preventing the proper orientation of the C-terminal helix and the folding of the C-terminal tail over the active site. Post-translational modifications (PTMs), such as phosphorylation, may release this autoinhibition by separating the N-tails, thereby enabling hinge motions of the N-terminal domain to accommodate NAD^+, while the C-terminal helix and C-tail realign to form a fully functional active site. Additionally, other PTMs, including acetylation and methylation within the N-terminal domain (**Table S1**), likely modulate NADK's conformational state and activity, providing a versatile regulatory mechanism responsive to cellular state.

In line with the key role of the flexible NADK tails in regulating its enzyme activity, numerous mutations are observed in both the N-terminal and C-terminal regions in cancer patients, as well as within the catalytic core (*27, 28*). However, further studies, including mutational analysis and investigations into their effects on tumorigenesis, are necessary to determine which mutations functionally alter NADK activity.

Finally, a structural comparison of various NADKs to date reveals an original phylogenetic evolution, as intriguingly, the cytosolic hsNADK shares more similarities with bacterial enzymes, particularly those from gram-negative pathogens, than the human mitochondrial variant (**Fig. S1**).

In summary, the high-resolution structure of the NADK-NAD^+ complex paves the way for in silico screening of chemical libraries and structure-based drug design to identify NADK inhibitors as potential drug candidates for cancer therapy.

MATERIALS AND METHODS

Reagents and antibodies

Adenosine triphosphate salt (ATP; Sigma-Aldrich, A2383), anti-FLAG M2 Affinity Gel (Sigma-Aldrich, A2220), 3X FLAG peptide BCA kit (ThermoFisher, 23225), Bradford assay reagent (Bio-Rad, 5000006), β-nicotinamide adenine dinucleotide hydrate (NAD^+; Sigma-Aldrich, N7004), D-glucose 6-phosphate disodium salt hydrate (G6P; Sigma-Aldrich, G7250), glucose 4 6-phosphate dehydrogenase from baker's yeast (G6PD; Sigma-Aldrich, G6378), KOD Xtreme™ Hot Start DNA Polymerase (Millipore, 71975-3), protease inhibitor cocktail (Sigma-Aldrich, P8340), HEPES (ThermoFisher, 15630080), HEPES (Sigma-Aldrich, H0887), PEI MAX® Linear Polyethylenimine Hydrochloride (Polysciences, 24765-1), InstantBlue® Coomassie Protein Stain (ISB1L) (ab119211), and SuperSignal™ West Pico PLUS Chemiluminescent Substrate (PI34580) are commercially available.

Commercially available antibodies, such as anti-FLAG antibody (Cell Signaling Technology Cat# 14793, RRID: AB_2572291; 1:1000 for WB), vinculin (Cell Signaling Technology Cat# 13901, RRID: AB_2728768; 1:1,000 for WB), and horse radish peroxidase (HRP)-conjugated secondary anti-rabbit (Cell Signaling Technology Cat# 7074, RRID:AB_2099233; 1:5,000) were used.

cDNA constructs for mammalian expression

Full-length human NADK isoform 1 (RC200544) and NADK isoform 3 (RC231219) with a C-terminal FLAG tagged were purchased from Origene and described previously (*10*). NADK and deletion variants were subcloned into pcDNA™FRT/TO vector with a C-terminal FLAG tag. Point mutations and several deletion variants (Δ81-90) were generated by site-detected mutagenesis using KOD Xtreme™ Hot Start DNA Polymerase, followed by DPN1 digestion of the parental DNA. All the different mutants of hsNADK used in this study were confirmed using the Sanger sequencing methods at the McDermott Center Sequencing Core at UT Southwestern Medical Center.

Engineering a stable variant of hsNADK

$NADK_{esv}$ amino acids sequence was derived from the full-length cytosolic human $NADK_{FL}$. (EC:2.7.1.23; Uniprot ID: O95544). The changes were as follows: 1) deletions of residues 1-67, 81-88, and the polyglutamate chain 436-444, 2) the substitutions of H89E, I90T, Q96V residues, and 3) S/T substitution of surface exposed cysteines, including C69S, C79T, C162T and C402T.

Bacterial expression and purification of full-length and an Engineered hsNADK

The synthetic genes coding for hsNADK and $NADK_{esv}$ were cloned in the plasmid pET22b to produce a recombinant C-terminal His-tagged protein. The resulting plasmid was transformed in BL21(DE3) (C2527 NEB), and bacteria were grown under aerobic conditions in LB at 37 °C with the appropriate antibiotics (ampicillin 100 µg/ml, chloramphenicol 34 µg/ml). The expression of the His-tagged $NADK_{esv}$ was induced during the exponential phase (OD_{600} 0.6-0.8) by adding 0.7 mM isopropyl-β-D-thiogalactopyranoside (IPTG), 5 h at 37 °C. Afterwards, bacterial cells were harvested by centrifugation at 6,000 g for 15 min at 8 °C, suspended in lysis buffer (50 mM Tris pH 7.8, 50 mM NaCl, 2 mM DTT) with 10 µg/ml lysozyme and a cocktail of protease inhibitors (cOmplete™, EDTA-free Protease Inhibitor cocktail, Roche Life Science, Germany), and the lysate was finally frozen at -40 °C for 72 h. Once thawed, the lysate was sonicated four times (6 min; 2 s pulses; amplitude 55; Sonicator BIOBLOCK Scientific Vibra Cell 72405) and clarified by centrifugation (18,000 g, 20 min, 8 °C). The supernatant was collected, passed through a 0.45 µm filter, and placed on the cOmplete™ His-Tag Purification Column (Roche® Life Science, Germany) previously equilibrated with 50 mM Tris pH 7.8, 50 mM NaCl, 2 mM DTT. The His-tagged protein was eluted with a linear gradient of imidazole (12-300 mM imidazole in 50 mM Tris pH 7.8, 50 mM NaCl, 2 mM DTT). The protein was subjected to size exclusion chromatography with a Superdex 200 column (GE Healthcare) equilibrated with 50 mM Tris pH 7.8, 50 mM NaCl,

2 mM DTT, and the presence and purity of $NADK_{esv}$ was confirmed by SDS-PAGE (Bolt™ 4-12%, Bis-Tris, Invitrogen™, USA).

Cell culture

The HEK-293 cells (a gift from Carol Mackintosh (University of Dundee)) were grown in DMEM (Corning 10-017-CV) supplemented with 10% fetal bovine serum (R&D Systems, S11550). The cells used for the experiments were tested regularly for mycoplasma.

Cell line-based purification of NADK for *in vitro* activity assays

Briefly, HEK-293 cells were seeded in 15 cm dishes for transfection. The next day, cells were transfected with 20 µg of plasmids using the polyethylenimine (PEI) transfection reagent according to the manufacturer's instructions. After the 36 hours post-transfection, cells were washed with ice-cold PBS and were lysed with 1% Triton lysis buffer (1% Triton X-100, 40 mM HEPES pH 7.4, 120 mM NaCl, 10 mM sodium pyrophosphate, 10 mM glycerol 2-phosphate, 1 mM EDTA and protease inhibitor cocktail (Sigma, P8340). Cell lysates were centrifuged at 21,000 g for 15 min at 4 °C. Next, cell lysates were further incubated with 30 µl of a 50% slurry of anti-FLAG M2 Affinity Gel for 4 hours at 4^{o}C and washed thrice with lysis buffer and once with equilibration buffer (10 mM HEPES, 50 mM NaCl, and protease inhibitors). NADK-FLAG was eluted in 50 µl elution buffer (0.2 mg/ml 3xFLAG peptide, 10 mM HEPES, 50 mM NaCl, protease inhibitors) for 1.5 hours at 4 °C. The eluted product was passed through 0.45 µm Costar® Spin-X® Centrifuge tube filters, and protein concentrations were determined with a Bradford assay (Biorad, 500-0006). For further confirmation, proteins were visualized with Coomassie staining.

Protein purification for Cryo-EM

Full-length NADK purified from mammalian cells: Full-length human NADK isoform 1 (RC200544) with a C-terminal FLAG tag was obtained from Origene. FLAG-tagged NADK was transiently transfected in HEK-293 cells. Cells were lysed with 1% Triton lysis buffer (1% Triton X-100, 40 mM HEPES, pH 7.4, 120 mM NaCl, 10 mM sodium pyrophosphate, 10 mM glycerol 2-phosphate, 1 mM EDTA) supplemented with 0.1% β-mercaptoethanol and protease inhibitor cocktail prior to cell lysis (*9, 29*). Eighty milligrams of protein was incubated with 1 ml of anti-FLAG M2 Affinity Gel for 4 hours, followed by three washes with 1% Triton lysis buffer containing 0.5 M NaCl, two washes with equilibration buffer (10 mM HEPES, 50 mM NaCl, and protease inhibitors), and subsequent elution with FLAG peptide (0.2 mg/ml 3xFLAG peptide, 10 mM HEPES, 50 mM NaCl, protease inhibitors)(*10*). The eluate was passed through 0.45 µm Costar® Spin-X® Centrifuge

Tube Filters before concentrating the samples using Amicon® Ultra columns (UFC501024). Samples were prepared at a concentration of 5 mg/ml in 10 mM HEPES, with 0.01% NP40, and 1 mM DTT, and further diluted for cryo-EM analysis.

Cryo-EM sample preparation and data acquisition

The protein samples were prepared and used as follows: Sample-1) $NADK_{FL}$: A 5 mg/ml stock was diluted to 0.2 mg/ml in 10 mM HEPES, 0.01% NP-40, and 1 mM DTT; Sample-2) stable $NADK_{esv}$ for the apo-structure: An 11 mg/ml stock was used at 0.3 mg/ml in 50 mM Tris (pH 7.8), 50 mM NaCl, and 2 mM DTT. Sample-3) $NADK_{esv}$-NAD^+ complex: Prepared at 0.55 mg/ml in 50 mM Tris (pH 7.8), 50 mM NaCl, 2 mM DTT, and 5 mM NAD^+.

The protein samples were then applied to Quantifoil 300 mesh R1.2/1.3 grids (Quantifoil, Sample-1 and 2) or C-flat 300 mesh R1.2/1.3 grids (EMS, Sample-3) pre-treated using a Pelco EasiGlow instrument (Ted Pella). The grid was flash-frozen into liquid ethane using a Vitrobot Mark IV (Thermo Fisher Scientific), with the following settings: blot time 3 s, wait time 3 s, relative humidity 95%, and 4 °C.
Grid screening was performed on a Talos Arctica or Talos Glacios microscope (Thermo Fisher Scientific) at the UTSW Cryo-Electron Microscopy Facility (CEMF). The best grid (from Sample-1 or Sample-2) was used for a 24-hour data collection on a Titan Krios microscope (Thermo Fisher Scientific) at CEMF, equipped with the post-column BioQuantum Imaging Filter (Gatan) and a K3 direct electron detector (Gatan) Sample-3 was collected similarly with the Selectris X Imaging Filter (Thermo Fisher Scientific) and a Falcon 4i direct electron detector (Thermo Fisher Scientific).

All using SerialEM (*31*), cryo-EM data of sample-1 and 2 were collected in super-resolution mode with a 20 eV energy filter slit, while sample-3 was collected with a 10 eV energy filter slit. For the full-length NADK, 6,013 movies were acquired at a pixel size of 0.415 Å. For $NADK_{esv}$-Apo, 6,732 movies were acquired at a pixel size of 0.417 Å. For $NADK_{esv}$-NAD^+ complex, 9,105 movies were acquired in EER format at a pixel size of 0.738 Å. The accumulated total dose was 50 $e^-/Å^2$ for each movie stack. The defocus range of the images was set to be −0.9 to −2.2 µm.

Cryo-EM data processing for full-length $NADK_{FL}$: Cryo-EM data were first processed in Relion (*32-34*) to obtain an initial map (data not shown) and used as the template for particle picking,

then using CryoSPARC (*35*). Raw movies were motion-corrected and dose-weighted, then averaged into single images with a binning factor of 2 using Patch Motion Correction, resulting in a pixel size of 0.83 Å/pixel. Contrast Transfer Function (CTF) parameters were estimated using Patch CTF Estimation. 5,779 micrographs were selected for further processing after manual curation. A total of 1,820,219 particles were picked and extracted and went through two rounds of 2D classification, from which 305,975 particles were selected. These particles were subjected to one round of 3D Heterogeneous Refinement, Non-Uniform Refinement, and Global CTF Refinement. It was then followed by another round of 3D Heterogeneous Refinement and 77,606 particles remained. A final Non-Uniform Refinement generated a reconstruction with an overall resolution of 3.18 Å, according to the gold-standard Fourier shell correlation (FSC) using the 0.143 criterion (*36*). Local resolution was estimated using CryoSPARC. The map was further processed with DeepEMhancer (36) for model building and refinement (**Fig. S9**).

Cryo-EM data processing for $NADK_{esv}$ (Apo): Cryo-EM data were processed using CryoSPARC (34). Raw movies were motion-corrected and dose-weighted, then averaged into single images with a binning factor of 2 using Patch Motion Correction, resulting in a pixel size of 0.834 Å/pixel. Contrast Transfer Function (CTF) parameters were estimated using Patch CTF Estimation. 5,901 micrographs were selected for further processing after manual curation. A total of 4,587,353 particles were extracted and went through two rounds of 2D classification, from which 543,841 particles were selected. These particles were subjected to one round of 3D Heterogeneous Refinement, and 316,309 remained. It is then followed by Global CTF Refinement, Homogeneous Refinement, and Non-Uniform Refinement, resulting in a reconstruction with an overall resolution of 2.81 Å, according to the gold-standard Fourier shell correlation (FSC) using the 0.143 criterion (*37*). Local resolution was estimated using Relion (*32-34*). The map was further processed with DeepEMhancer (*36*) for model building and refinement (**Fig. S10).**

Cryo-EM data processing for $NADK_{esv}$-NAD^+ complex: Cryo-EM data were processed using CryoSPARC (*35*). Raw movies were motion-corrected and dose-weighted, then averaged into single images. Contrast Transfer Function (CTF) parameters were estimated using Patch CTF Estimation. 7,007 micrographs were selected for further processing after manual curation. A structure obtained from CryoSPARC-Live (*35*) was used as the template for particle picking. A total of 1,716,164 particles were extracted and went through two rounds of 2D classification, from which 451,850 particles were selected. These particles were subjected to one round of 3D Heterogeneous Refinement, and 251,813 remained. It is then followed by Homogeneous Refinement, Non-

Uniform Refinement, Global CTF Refinement, and Local CTF Refinement, resulting in a reconstruction with an overall resolution of 2.34 Å, according to the gold-standard Fourier shell correlation (FSC) using the 0.143 criterion (*37*). Local resolution was estimated using CryoSPARC(*35*). The map was further processed with DeepEMhancer (*36*) for model building and refinement (**Fig. S11**).

In-vitro enzymatic activity assay on bacterially expressed hsNADK

The *in vitro* enzymatic activities of $NADK_{FL}$ (*E. Coli*) and $NADK_{esv}$ (*E. Coli*) were assessed using a glucose-6-phosphate dehydrogenase-coupled assay (*10*). Final concentrations were 5 mM MgATP, 5 mM glucose-6-phosphate, 0.1-2 mM NAD^+ (12 different concentrations), 1 U/ml G6PD and 25 nM NADK in 50 mM BisTris pH 7.0, 100 mM NaCl, and 1 mM $MgCl_2$ in a final volume of 100 µl. Experiments were carried out at 30 °C in UV-Star 96 half-well plates (Greiner) in a CLARIOstar plate reader (BMG Labtech), measuring A340 every 32 seconds for 30 min after enzyme addition. A340 was converted into NADH concentration, using an absorption coefficient of 6.22 $mM^{-1} \cdot cm^{-1}$. The steady-state rate constant, k_{ss}, was determined at each NAD^+ concentration by linear regression of the initial reaction phase (10 first minutes). Catalytic rate constants, k_{cat}, and K_M values were obtained by fitting the dependence of k_{ss} on NAD^+ concentration using a hyperbolic function in GraFit software (Erithacus Software Ltd, version 7.0.3).

In-vitro enzymatic activity assay for hsNADK expressed in mammalian cells

The *in vitro* enzymatic activity of hsNADK was assayed using the glucose 6-phosphate dehydrogenase-coupling assay, as previously described (*10*). Briefly, for each reaction, approximately 0.8 µg of purified NADK or NADK variants were subjected to an enzymatic assay that couples its generation of $NADP^+$ to G6PD-mediated production of NADPH, which is then measured as a change in A340 over time.

Experiments were carried out at 37 °C in SpectraMax iD3- Microplate reader (Molecular devices) with a final volume of 100 µl. The assay was performed in a 100 µl reaction in a 96-well plate containing 10 mM ATP, 10 mM glucose-6-phosphate, 0.5 U G6PD, 10 mM $MgCl_2$, 100 mM Tris-HCl (pH 8.0), and 2 mM of NAD^+. Measurements of A340 were made every 2 minutes for 20 min at 37 °C. A control reaction containing all the components except the enzyme (no NADK) was included. The presented data shows normalized absorbance (O.D.), with the control (no enzyme) subtracted.

PTM analysis by Mass Spectrometry

HEK-293 cells (10 x 15 cm dishes) were transiently transfected with NADK-FLAG (20 µg per 15 cm dish) and cultured in DMEM supplemented with 10% FBS. After 48 hours post-transfection, cells were lysed with 1% Triton X-100 in lysis buffer, and NADK-FLAG was immunoprecipitated using anti-FLAG M2 Affinity Gel (Sigma-Aldrich, A2220) for 3.5 hours. The beads were washed three times with lysis buffer, followed by two washes with elution buffer (10 mM HEPES, 50 mM NaCl, protease inhibitors, and 1 µM Microcystin). NADK-FLAG was then eluted by incubating the beads in elution buffer containing 0.2 mg/mL 3xFLAG peptide for 1.5 hours at 4°C. The eluate was subjected to SDS PAGE run and Coomassie Blue staining (Abcam, ab119211). The NADK band was excised and samples were then processed for PTM analysis as previously described (*18*).

Thermal shift assay for hsNADK

Thermal denaturation was performed in duplicate by increasing the temperature from 25 to 93 °C in a qRT-PCR device (Mx3005P, Stratagene) using a SYAL emission filter at a gain of 8. The final concentrations were 2 µM NADK, 5× Sypro Orange (Sigma), 10 mM ligand in 50 mM BisTris pH 7.0, 100 mM NaCl and 1 mM $MgCl_2$ and in a final volume of 20 µl. Melting temperature values (T_m) were determined using the *wTSA-CRAFT* web server (https://bioserv.cbs.cnrs.fr/TSA_CRAFT/) (*30*).

Limited Proteolysis

10 µl of 0.2 mg/ml of protein (without or with 5 mM of NAD^+) were incubated with 10 µl of 0.01 mg/ml of different proteases (α-Chymotrypsin, Endoproteinase Glu-C, Elastase, Trypsin, Thermolysin, Bromelain, Pepsin, Clostripain, Actinase-E and Subtilisin from Hampton Research) at 37 °C during 1 h. Laemmli buffer was then added to the reaction, the mix was heated 5 min at 95 °C and deposed on SDS-PAGE (Bolt™ 4-12%, Bis-Tris, Invitrogen™, USA).

Isothermal titration calorimetry on bacterially expressed hsNADK

The enzymes were purified in a buffer containing 50 mM HEPES pH 7.8, 50 mM NaCl and 5 mM DTT, and ligand solutions were prepared in the same buffer plus an equimolar concentration of $MgCl_2$. Experiments were carried out at 25 °C in a MicroCal PEAQ-ITC device (Malvern Panalytical). The enzyme was used at a final concentration of 300 µM in the ITC cell and the ligands at 5 mM in the syringe. Titrations consisted of 30 injections of 1 µl of ligand every 150 s

with a stir speed of 750 rpm. K_d values were determined using the MicroCal PEAQ-ITC analysis software version 1.41.

Mass Photometry

Mass Photometry was performed as previously described (*18*). Engineered NADK ($NADK_{esv}$) purified from *E. coli* (stock 11 mg/ml) was diluted in PBS to make a 1 µM. Prior to mass photometry measurements, it was further diluted 1:10 in PBS (final concentration of 0.1 µM). For each measurement, 2 µl of protein was used, and 60-second movies were recorded. Data were analyzed using DiscoverMP (Refeyn).

Western blotting

Western blotting was performed as previously described (*10, 29, 38*). Cells were lysed in ice-cold 1% Triton cell lysis buffer. After determining the protein concentration using a Bio-Rad Protein Assay kit (Bio-Rad, 5000006), 15 µg of protein were separated by SDS-PAGE and transferred to nitrocellulose membranes (Bio-Rad, 1620112). The membranes were blocked with 5% non-fat milk for 1 hour at room temperature (RT), incubated overnight with primary antibodies, followed by incubation with HRP-conjugated secondary antibodies. Finally, a chemiluminescence detection reagent was used to visualize the proteins.

Isotope tracing for *de novo* $NADP^+$ generation

HEK-293 NADK knockout cells ($400x10^3$ cells/well) were grown in six-well plates overnight followed by transfection with 3 µg of various NADK variants using transfection reagent according to the manufacturer's instructions. 24 h post-transfection, cells were subjected to isotope tracing in nicotinamide-free media supplemented with 10% dialyzed serum and 0.2 mg/ml [2,4,5,6-2H] nicotinamide (Cambridge Isotope Laboratories, DLM-6883-PK) for 2 h. Metabolites were extracted in 200 µl of ice-cold extraction buffer (MeOH: acetonitrile: water in a 40:40:20 ratio). The tubes were incubated on ice for 15 min and centrifuged at 20,000 g for 10 min at 4 °C. Supernatants were collected and subjected to liquid chromatography-mass spectrometry (LC-MS). $NADP^+$ and NADPH were chromatographically resolved as described previously(*18, 39*). Tracing $^2H_4$-nicotinamide into these metabolites was achieved with a Thermo Lumos 1M tribrid mass spectrometer operated in a selected ion monitoring (SIM) scan mode, switching between positive and negative polarities. The mass spectrometer collected data with a resolving power of 500,000 FWHM to resolve the deuterium-labeled metabolite from its naturally abundant $^{13}C_4$ isotope. All analytes in our SIM scans were isolated with a 13-dalton window with no offset. This

wide isolation window ensured we could capture all predicted isotopologues and any naturally occurring isotopologues in our labeling strategy. The AGC target for these scans was set to 100%, and the maximum injection time was set to Auto to maximize method efficiency. We used the following m/z values for our inclusion lists: 664.1164 (NAD^+, positive mode), 744.0827 ($NADP^+$, positive mode), 664.11675 (NADH, negative mode), and 744.0838 (NADPH, negative mode). SIM scans were not scheduled and cycled throughout the method. Source conditions were the same as described in our previously reported papers (*18*). Data were analyzed using the Thermo Scientific TraceFinder 5.1 software package. Theoretical m/z values were calculated out to M+10 for ^2H isotopologues by using the exact mass shift of a hydrogen atom to a deuterium atom (1.0063) and the data processing criteria described previously (*40*). For normalization of each sample, the insoluble pellet from the metabolite extractions was solubilized with 8 M urea in 10 mM Tris (pH 8), and the protein was quantified with a BCA assay kit. The data is presented as normalized peak area; each data point is the mean± S.E.M. of three biological replicates. Experiments are representative of at least two independent experiments.

Phylogenetic Analysis of NADKs.

The multiple sequence alignments of various NADKs shown in Fig. S1 were generated using Espript (https://espript.ibcp.fr/ESPript/ESPript/) (*41*). The phylogenic tree of various NADKs was built using the software Ibis2Analyzer (http://ibis2analyzer.lcqb.upmc.fr/) (*42*).

Statistical analysis

The GraphPad Prism 10 is used for all the statistical analysis. For comparative analysis, two-tailed Student's t-tests were used for two conditions, and ANOVA analyses were used for experiments with more than two conditions to determine significance. Data are from at least three independent experiments and represented as the mean ± S.E.M. (standard error of the mean) of individual data points.

REFERENCES

1. N. Pollak, C. Dölle, M. Ziegler, The power to reduce: pyridine nucleotides--small molecules with a multitude of functions. Biochem J 402, 205-218 (2007).
2. H. Q. Ju, J. F. Lin, T. Tian, D. Xie, R. H. Xu, NADPH homeostasis in cancer: functions, mechanisms and therapeutic implications. *Signal Transduct Target Ther* **5**, 231 (2020).
3. N. S. Chandel, NADPH-The Forgotten Reducing Equivalent. *Cold Spring Harb Perspect Biol* **13**, (2021).
4. G. Hoxhaj, B. D. Manning, The PI3K-AKT network at the interface of oncogenic signalling and cancer metabolism. *Nat Rev Cancer* **20**, 74-88 (2020).
5. A. A. Pramono, G. M. Rather, H. Herman, K. Lestari, J. R. Bertino, NAD- and NADPH-Contributing Enzymes as Therapeutic Targets in Cancer: An Overview. *Biomolecules* **10**, (2020).
6. K. Ohashi, S. Kawai, K. Murata, Identification and characterization of a human mitochondrial NAD kinase. *Nat Commun* **3**, 1248 (2012).
7. F. Lerner, M. Niere, A. Ludwig, M. Ziegler, Structural and functional characterization of human NAD kinase. *Biochem Biophys Res Commun* **288**, 69-74 (2001).
8. N. Pollak, M. Niere, M. Ziegler, NAD kinase levels control the NADPH concentration in human cells. *J Biol Chem* **282**, 33562-33571 (2007).
9. D. H. Tran, R. Kesavan, H. Rion, M. H. Soflaee, A. Solmonson, D. Bezwada, H. S. Vu, F. Cai, J. A. Phillips, 3rd, R. J. DeBerardinis, G. Hoxhaj, Mitochondrial NADP(+) is essential for proline biosynthesis during cell growth. *Nat Metab* **3**, 571-585 (2021).
10. G. Hoxhaj, I. Ben-Sahra, S. E. Lockwood, R. C. Timson, V. Byles, G. T. Henning, P. Gao, L. M. Selfors, J. M. Asara, B. D. Manning, Direct stimulation of NADP(+) synthesis through Akt-mediated phosphorylation of NAD kinase. *Science* **363**, 1088-1092 (2019).
11. T. Schild, M. R. McReynolds, C. Shea, V. Low, B. E. Schaffer, J. M. Asara, E. Piskounova, N. Dephoure, J. D. Rabinowitz, A. P. Gomes, J. Blenis, NADK is activated by oncogenic signaling to sustain pancreatic ductal adenocarcinoma. *Cell Rep* **35**, 109238 (2021).
12. R. Rabani, C. Cossette, F. Graham, W. S. Powell, Protein kinase C activates NAD kinase in human neutrophils. *Free Radic Biol Med* **161**, 50-59 (2020).
13. Z. Liang, T. Liu, Q. Li, G. Zhang, B. Zhang, X. Du, J. Liu, Z. Chen, H. Ding, G. Hu, H. Lin, F. Zhu, C. Luo, Deciphering the functional landscape of phosphosites with deep neural network. *Cell Rep* **42**, 113048 (2023).
14. P. M. Tedeschi, N. Bansal, J. E. Kerrigan, E. E. Abali, K. W. Scotto, J. R. Bertino, NAD+ Kinase as a Therapeutic Target in Cancer. *Clin Cancer Res* **22**, 5189-5195 (2016).
15. Y. H. Tsang, T. Dogruluk, P. M. Tedeschi, J. Wardwell-Ozgo, H. Lu, M. Espitia, N. Nair, R. Minelli, Z. Chong, F. Chen, Q. E. Chang, J. B. Dennison, A. Dogruluk, M. Li, H. Ying, J. R. Bertino, M. C. Gingras, M. Ittmann, J. Kerrigan, K. Chen, C. J. Creighton, K. Eterovic, G. B. Mills, K. L. Scott, Functional annotation of rare gene aberration drivers of pancreatic cancer. *Nat Commun* **7**, 10500 (2016).
16. D. Ilter, S. Drapela, T. Schild, N. P. Ward, E. Adhikari, V. Low, J. Asara, T. Oskarsson, E. K. Lau, G. M. DeNicola, M. R. McReynolds, A. P. Gomes, NADK-mediated de novo NADP(H) synthesis is a metabolic adaptation essential for breast cancer metastasis. *Redox Biol* **61**, 102627 (2023).
17. Z. Zeng, J. Gao, T. Chen, Z. Zhang, M. Li, Q. Fan, G. Liu, X. Li, Z. Li, C. Zhong, F. Yao, L. Sun, Y. Deng, M. Li, Nicotinamide adenine dinucleotide kinase promotes lymph node metastasis of NSCLC via activating ID1 expression through BMP pathway. *Int J Biol Sci* **19**, 3184-3199 (2023).
18. C. Mary, M. H. Soflaee, R. Kesavan, M. Gelin, H. Brown, G. Zacharias, T. P. Mathews, A. Lemoff, C. Lionne, G. Labesse, G. Hoxhaj, Crystal structure of human NADK2 reveals a

dimeric organization and active site occlusion by lysine acetylation. *Mol Cell* **82**, 3299-3311 (2022).
19. J. Du, M. Estrella, K. Solorio-Kirpichyan, P. D. Jeffrey, A. Korennykh, Structure of human NADK2 reveals atypical assembly and regulation of NAD kinases from animal mitochondria. *Proc Natl Acad Sci U S A* **119**, e2200923119 (2022).
20. N. R. Love, N. Pollak, C. Dolle, M. Niere, Y. Chen, P. Oliveri, E. Amaya, S. Patel, M. Ziegler, NAD kinase controls animal NADP biosynthesis and is modulated via evolutionarily divergent calmodulin-dependent mechanisms. *Proc Natl Acad Sci U S A* **112**, 1386-1391 (2015).
21. G. Poncet-Montange, L. Assairi, S. Arold, S. Pochet, G. Labesse, NAD kinases use substrate-assisted catalysis for specific recognition of NAD. *J Biol Chem* **282**, 33925-33934 (2007).
22. T. Ando, K. Ohashi, A. Ochiai, B. Mikami, S. Kawai, K. Murata, Structural determinants of discrimination of NAD+ from NADH in yeast mitochondrial NADH kinase Pos5. *J Biol Chem* **286**, 29984-29992 (2011).
23. J. Jumper, R. Evans, A. Pritzel, T. Green, M. Figurnov, O. Ronneberger, K. Tunyasuvunakool, R. Bates, A. Zidek, A. Potapenko, A. Bridgland, C. Meyer, S. A. A. Kohl, A. J. Ballard, A. Cowie, B. Romera-Paredes, S. Nikolov, R. Jain, J. Adler, T. Back, S. Petersen, D. Reiman, E. Clancy, M. Zielinski, M. Steinegger, M. Pacholska, T. Berghammer, S. Bodenstein, D. Silver, O. Vinyals, A. W. Senior, K. Kavukcuoglu, P. Kohli, D. Hassabis, Highly accurate protein structure prediction with AlphaFold. *Nature* **596**, 583-589 (2021).
24. P. V. Hornbeck, B. Zhang, B. Murray, J. M. Kornhauser, V. Latham, E. Skrzypek, PhosphoSitePlus, 2014: mutations, PTMs and recalibrations. *Nucleic Acids Res* **43**, D512-520 (2015).
25. L. Liu, X. Su, W. J. Quinn, 3rd, S. Hui, K. Krukenberg, D. W. Frederick, P. Redpath, L. Zhan, K. Chellappa, E. White, M. Migaud, T. J. Mitchison, J. A. Baur, J. D. Rabinowitz, Quantitative Analysis of NAD Synthesis-Breakdown Fluxes. *Cell Metab* **27**, 1067-1080 e1065 (2018).
26. R. Rahimova, P. Nogaret, V. Huteau, M. Gelin, D. A. Clement, G. Labesse, S. Pochet, A. B. Blanc-Potard, C. Lionne, Structure-based design, synthesis and biological evaluation of a NAD(+) analogue targeting Pseudomonas aeruginosa NAD kinase. *FEBS J* **290**, 482-501 (2023).
27. E. Cerami, J. Gao, U. Dogrusoz, B. E. Gross, S. O. Sumer, B. A. Aksoy, A. Jacobsen, C. J. Byrne, M. L. Heuer, E. Larsson, Y. Antipin, B. Reva, A. P. Goldberg, C. Sander, N. Schultz, The cBio cancer genomics portal: an open platform for exploring multidimensional cancer genomics data. *Cancer Discov* **2**, 401-404 (2012).
28. J. Gao, B. A. Aksoy, U. Dogrusoz, G. Dresdner, B. Gross, S. O. Sumer, Y. Sun, A. Jacobsen, R. Sinha, E. Larsson, E. Cerami, C. Sander, N. Schultz, Integrative analysis of complex cancer genomics and clinical profiles using the cBioPortal. *Sci Signal* **6**, pl1 (2013).
29. D. H. Tran, D. Kim, R. Kesavan, H. Brown, T. Dey, M. H. Soflaee, H. S. Vu, A. Tasdogan, J. Guo, D. Bezwada, H. Al Saad, F. Cai, A. Solmonson, H. Rion, R. Chabatya, S. Merchant, N. J. Manales, V. T. Tcheuyap, M. Mulkey, T. P. Mathews, J. Brugarolas, S. J. Morrison, H. Zhu, R. J. DeBerardinis, G. Hoxhaj, De novo and salvage purine synthesis pathways across tissues and tumors. *Cell* **187**, 3602-3618 (2024).
30. V. Reys, J. Kowalewski, M. Gelin, C. Lionne, wTSA-CRAFT: an open-access web server for rapid analysis of thermal shift assay experiments. *Bioinform Adv* **3**, vbad136 (2023).
31. D. N. Mastronarde, Automated electron microscope tomography using robust prediction of specimen movements. *J Struct Biol* **152**, 36-51 (2005).

32. S. H. Scheres, RELION: implementation of a Bayesian approach to cryo-EM structure determination. *J Struct Biol* **180**, 519-530 (2012).
33. R. Fernandez-Leiro, S. H. W. Scheres, A pipeline approach to single-particle processing in RELION. *Acta Crystallogr D Struct Biol* **73**, 496-502 (2017).
34. S. H. W. Scheres, Amyloid structure determination in RELION-3.1. *Acta Crystallogr D Struct Biol* **76**, 94-101 (2020).
35. A. Punjani, J. L. Rubinstein, D. J. Fleet, M. A. Brubaker, cryoSPARC: algorithms for rapid unsupervised cryo-EM structure determination. *Nat Methods* **14**, 290-296 (2017).
36. R. Sanchez-Garcia, J. Gomez-Blanco, A. Cuervo, J. M. Carazo, C. O. S. Sorzano, J. Vargas, DeepEMhancer: a deep learning solution for cryo-EM volume post-processing. *Commun Biol* **4**, 874 (2021).
37. R. Henderson, A. Sali, M. L. Baker, B. Carragher, B. Devkota, K. H. Downing, E. H. Egelman, Z. Feng, J. Frank, N. Grigorieff, W. Jiang, S. J. Ludtke, O. Medalia, P. A. Penczek, P. B. Rosenthal, M. G. Rossmann, M. F. Schmid, G. F. Schroder, A. C. Steven, D. L. Stokes, J. D. Westbrook, W. Wriggers, H. Yang, J. Young, H. M. Berman, W. Chiu, G. J. Kleywegt, C. L. Lawson, Outcome of the first electron microscopy validation task force meeting. *Structure* **20**, 205-214 (2012).
38. M. H. Soflaee, R. Kesavan, U. Sahu, A. Tasdogan, E. Villa, Z. Djabari, F. Cai, D. H. Tran, H. S. Vu, E. S. Ali, H. Rion, B. P. O'Hara, S. Kelekar, J. H. Hallett, M. Martin, T. P. Mathews, P. Gao, J. M. Asara, B. D. Manning, I. Ben-Sahra, G. Hoxhaj, Purine nucleotide depletion prompts cell migration by stimulating the serine synthesis pathway. *Nat Commun* **13**, 2698 (2022).
39. A. B. Aurora, V. Khivansara, A. Leach, J. G. Gill, M. Martin-Sandoval, C. Yang, S. Y. Kasitinon, D. Bezwada, A. Tasdogan, W. Gu, T. P. Mathews, Z. Zhao, R. J. DeBerardinis, S. J. Morrison, Loss of glucose 6-phosphate dehydrogenase function increases oxidative stress and glutaminolysis in metastasizing melanoma cells. *Proc Natl Acad Sci U S A* **119**, (2022).
40. B. Faubert, A. Tasdogan, S. J. Morrison, T. P. Mathews, R. J. DeBerardinis, Stable isotope tracing to assess tumor metabolism in vivo. *Nat Protoc* **16**, 5123-5145 (2021).
41. X. Robert, P. Gouet, Deciphering key features in protein structures with the new ENDscript server. *Nucleic Acids Res* **42**, W320-324 (2014).
42. F. Oteri, E. Sarti, F. Nadalin, A. Carbone, iBIS2Analyzer: a web server for a phylogeny-driven coevolution analysis of protein families. *Nucleic Acids Res* **50**, W412-W419 (2022).

Acknowledgements

We thank the Structural Biology Laboratory and the Cryo-Electron Microscopy Facility at UT Southwestern Medical Center, partially supported by grant RP220582 from the Cancer Prevention & Research Institute of Texas (CPRIT), for their assistance with cryo-EM studies. We also thank the CRI Metabolomics Core, supported by the CPRIT Core Facilities Award RP240494, for help with LC-MS-based studies and the Proteomics Core at UT Southwestern Medical Center for assistance with proteomics. Special thanks to Chad Brautigam and Shih-Chia Tso for their assistance with mass photometry. Some data in this study were acquired with a mass photometer, supported by award S10OD030312-01 from the National Institutes of Health. We thank Angélique Devisch for her assistance with hsNADK purification and Stefano Trapani for providing in-house software to compute and draw rotation axes in PyMOL.

Funding

This research was supported by grants from the NIH: R01GM143236 (G.H.), Welch Foundation awards (I-2067-20210327 and I-2067-20240404 (G.H)); G.H. is a recipient of a Pew-Stewart Scholar; CPRIT Scholar (CPRIT; RR190087); and ACS Scholar awards (RSG-22-177-01-TBE). This work was also supported by the CNRS, the INSERM, and by grants from the ANR (ANR-17-CE18-0011 and ANR-20-CE18-0025) and the charity FRM (EQU202303016265).

Author Contributions

Conceptualization: GH, GL
Methodology: PPP, YL, CM, MHS, HT, HR, AL, LGZ, JSP, TPM
Investigation: PPP, CM, YL, MHS, KR, DK, DT, TD, MG, CL
Visualization: PPP, YL, CM, ZC
Supervision: GH, GL
Writing—original draft: PPP, CM, GH, GL
Writing—review & editing: GH, GL

Competing Interest Statement

None to be declared.

Data Availability

X-ray and diffraction data and coordinates have been deposited in the Protein Data Bank (PDB; accession no. 9CR3, 9CR4, and 9CRA). All other study data are included in the article and/or SI Appendix.

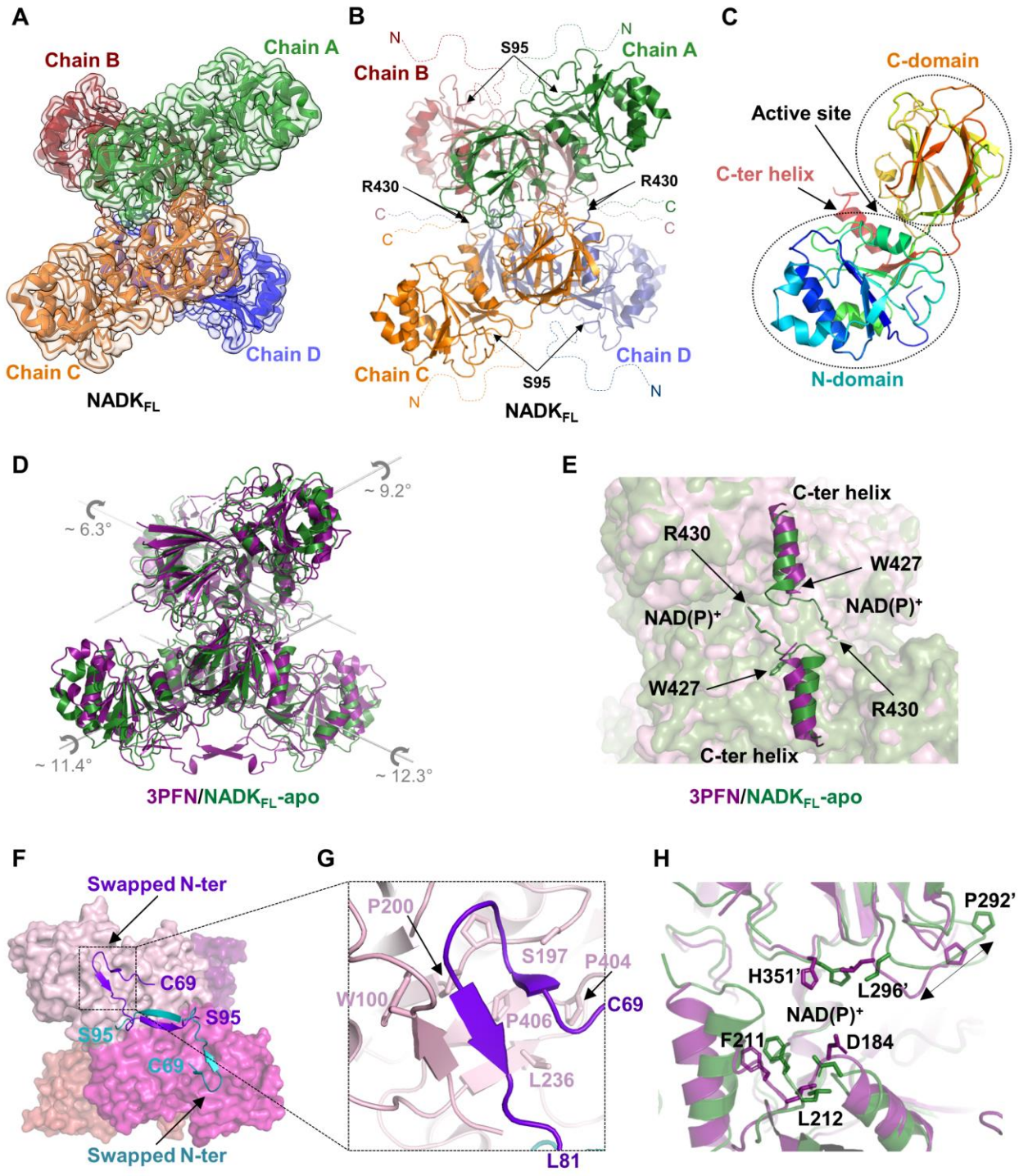
A
Chain B
Chain A
Chain C
Chain D
NADK$_{FL}$
B
N
S95
Chain A
Chain B
R430
R430
C
C
C
C
Chain C
Chain D
S95
N
N
NADK$_{FL}$
C
C-domain
Active site
C-ter helix
N-domain
D
~ 9.2°
~ 6.3°
~ 11.4°
~ 12.3°
3PFN/NADK$_{FL}$-apo
E
C-ter helix
R430
W427
NAD(P)$^+$
NAD(P)$^+$
W427
R430
C-ter helix
3PFN/NADK$_{FL}$-apo
F
Swapped N-ter
C69
S95
S95
C69
Swapped N-ter
G
P200
S197
P404
W100
C69
P406
L236
L81
H
P292'
H351'
L296'
NAD(P)$^+$
F211
D184
L212

Fig. 1. Cryo-EM structure of full-length human NADK revealing a tetrameric architecture.

(**A**) Cryo-EM structure of hsNADK$_{FL}$ purified from mammalian cells, revealing a tetrameric organization. Tetrameric NADK is shown embedded within its electron density, with each monomer in a distinct color that are labeled as Chains A-D.

(**B**) The organization of the tetrameric hsNADK$_{FL}$ is depicted with each monomer shown in a distinct color as in panel A, and their disordered tails are indicated by dashed lines. The boundaries of the catalytic domain visible in the cryo-EM structure are indicated by arrows showing the first (S95) and last (R430) residues, modeled in the density for the N-tail and C-tail, respectively.

(**C**) Domain organization of hsNADK$_{FL}$, showing the N-terminal domain, the C-terminal domain, the C-terminal helix (residues 413-424), and the position of the active site. The monomer is color in rainbow from its N-terminal (blue) to its C-terminal (red).

(**D**) Comparison of the apo hsNADK$_{FL}$ cryo-EM structure in green and the crystal structure of a truncated construct of hsNADK (PDB3PFN; unpublished) in violet. The rotation axis for each monomer is shown.

(**E**) Comparison of the orientation of the C-terminal helix (residues 413-424) in the crystal structure of hsNADK (3PFN) (violet) and the hsNADK$_{FL}$ cryo-EM structure (green).

(**F**) Illustration of the domain swapping for the N-tail (residues 69-94) shown in violet and blue in the crystal structure 3PFN. NADK monomers are shown in different shades of pink.

(**G**) Zoom of the contacts between the catalytic domain (pink ribbon) and the swapped N-tail (in violet ribbon).

(**H**) Close-up of the active site of NADK from the 3PFN and cryo-EM structures, showing the indicated structural rearrangements. The black double arrow highlights the translation of P292.

Panels A-H were drawn in PyMOL.

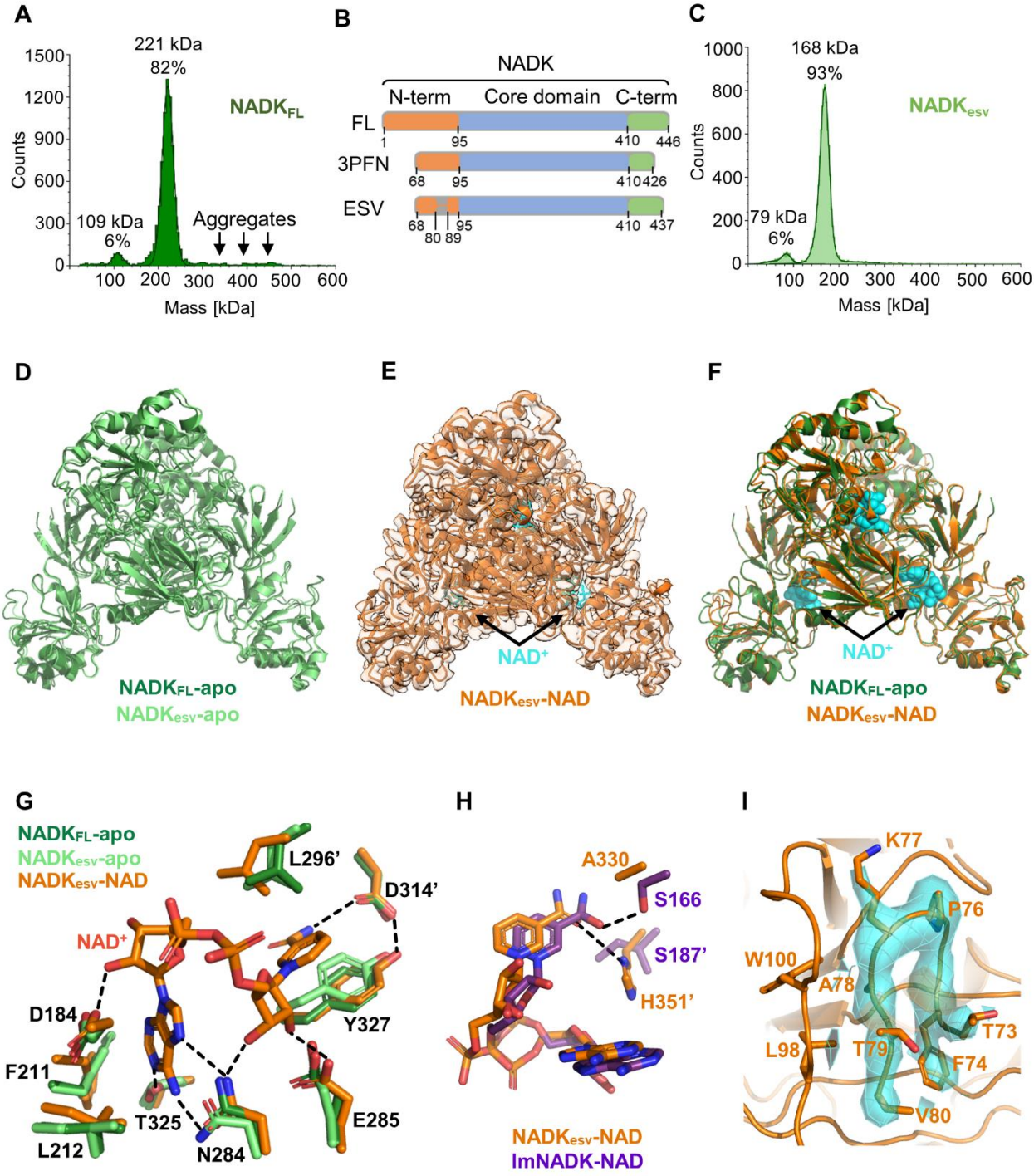
A
221 kDa
82%
NADK$_{FL}$
109 kDa
6%
Aggregates
Counts
Mass [kDa]
B
NADK
N-term
Core domain
C-term
FL
3PFN
ESV
C
168 kDa
93%
NADK$_{esv}$
79 kDa
6%
D
NADK$_{FL}$-apo
NADK$_{esv}$-apo
E
NAD$^+$
NADK$_{esv}$-NAD
F
NAD$^+$
NADK$_{FL}$-apo
NADK$_{esv}$-NAD
G
NADK$_{FL}$-apo
NADK$_{esv}$-apo
NADK$_{esv}$-NAD
L296'
D314'
NAD$^+$
D184
F211
L212
T325
N284
Y327
E285
H
A330
S166
S187'
H351'
NADK$_{esv}$-NAD
ImNADK-NAD
I
K77
P76
W100
A78
T73
L98
T79
F74
V80

Fig. 2. Cryo-EM structures of the engineered stable variant, hsNADK$_{esv}$, in apo and NAD$^+$-bound forms.

(**A**) Mass photometry of hsNADK$_{FL}$ purified from HEK293 cells, showing a tetrameric NADK (82%) with some high molecular weight aggregates.

(**B**) Schematic of the various constructs of hsNADK (wild-type, PDB3PFN, hsNADK$_{esv}$). The catalytic domain is shown in blue, the N-tail in orange, and the C-tail in green (including the very C-terminal helix).

(**C**) Mass photometry of hsNADK$_{esv,}$ showing a predominant tetramer (93%).

(**D**) Superimposition of the cryo-EM structures of the apo-forms of hsNADK$_{esv}$ (light green ribbons) and hsNADK$_{FL}$ (dark green ribbon), indicating subtle differences.

(**E**) The cryo-EM structure of the NAD$^+$-bound form of hsNADK$_{esv}$ in orange ribbons and sticks is displayed embedded in its electron density. The NAD$^+$ molecule is shown in cyan.

(**F**) Superimposition of the cryo-EM structures of the apo-form of hsNADK$_{FL}$ (dark green ribbon) and the NAD$^+$-bound form of hsNADK$_{esv}$ (orange ribbons). The NAD$^+$ molecule is shown in cyan spheres.

(**G**) Interactions between hsNADK and the bound NAD$^+$ molecule. Hydrogen bonds are shown as dashed lines.

(**H**) Comparison of the recognition of the amide group of the nicotinamide moiety in hsNADK$_{esv}$ (orange ribbons and sticks) and in the bacterial NADK from *Listeria monocytogenes* (PDB2I29) (violet ribbons and sticks).

(**I**) Electron density of the N-tail: The electron density for the visible part of the N-tail (residues 73-80) in the NAD$^+$-bound NADK$_{esv}$ structure is shown in orange surface and mesh. The backbone and side chains are depicted as sticks, while the rest of the structure is shown in orange ribbon.

Panels D,F,G were drawn using PyMOL.

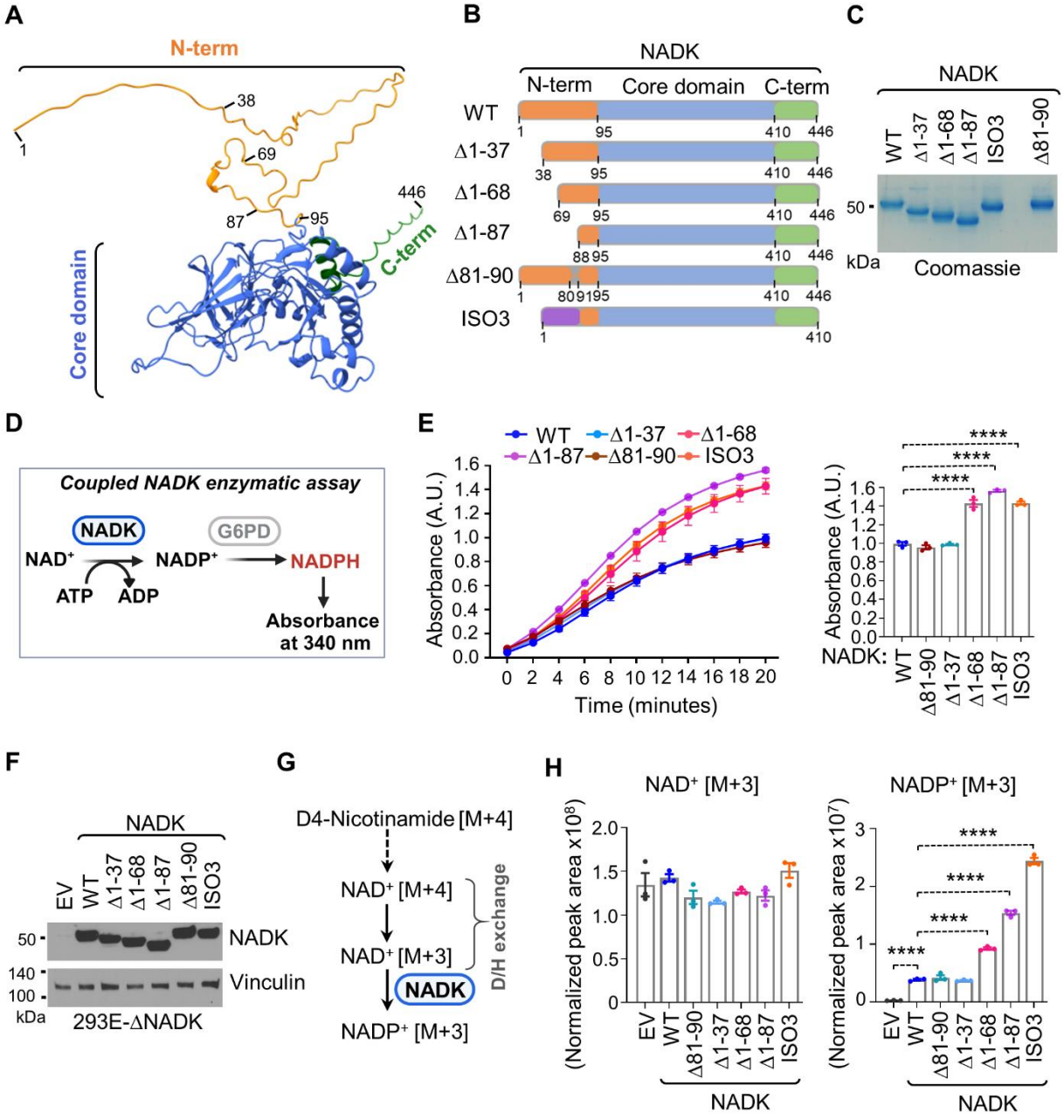
A
N-term
38
1
69
87
95
446
C-term
Core domain
B
NADK
N-term
Core domain
C-term
WT
Δ1-37
Δ1-68
Δ1-87
Δ81-90
ISO3
1
95
410
446
38
69
88
80
91
C
NADK
WT
Δ1-37
Δ1-68
Δ1-87
ISO3
Δ81-90
50
kDa
Coomassie
D
Coupled NADK enzymatic assay
NADK
G6PD
NAD+
NADP+
NADPH
ATP
ADP
Absorbance at 340 nm
E
WT
Δ1-37
Δ1-68
Δ1-87
Δ81-90
ISO3
Absorbance (A.U.)
Time (minutes)
****
NADK:
F
NADK
EV
WT
Δ1-37
Δ1-68
Δ1-87
Δ81-90
ISO3
50
140
100
kDa
NADK
Vinculin
293E-ΔNADK
G
D4-Nicotinamide [M+4]
NAD+ [M+4]
NAD+ [M+3]
NADK
NADP+ [M+3]
D/H exchange
H
NAD+ [M+3]
NADP+ [M+3]
(Normalized peak area x10^8)
(Normalized peak area x10^7)
****
NADK

Fig. 3. Disordered N-terminal domain inhibits NADK activity and cellular $NADP^+$ biosynthesis.

(**A**) Ribbon structure of NADK showing the disordered N-terminus (1-95) in orange, the kinase domain (96-429) in blue, and the C-terminal (410-446) region in green. PyMOL was used to depict the various regions using the AlphaFold model of human NADK.

(**B**) Schematics of NADK (full length) or various deletion (Δ) variants, including ∆1-37, ∆1-68, ∆1-87, ∆81-90, and isoform 3 (ISO3). The N-terminus domain is depicted in (orange), the kinase domain in blue, and C-terminus in green.

(**C**) Coomassie blue staining of the indicated purified NADK variants from HEK-293 cells.

(**D**) Schematics of the coupled NADK enzymatic assay. The absorbance of NADPH is detected at A340.

(**E**) *In vitro* enzymatic activity assay for the indicated immunopurified NADK variants (WT, ∆1-37, ∆1-68, ∆1-87, ∆81-90, and Iso3). Bar graphs show A340 values after 20 min of the reaction. The absorbance values are indicated as the mean ± S.E.M. of biological triplicates. The data is representative of three independent experiments. ****$p < 0.001$ was calculated with one-way ANOVA.

(**F**) Immunoblotting from NADK-deficient HEK-293 cells expressing either empty vector (EV) or the indicated NADK variants (WT, ∆1-37, ∆1-68, ∆1-87, ∆81-90, and ISO3).

(**G**) Schematics of labeling of NAD^+ and $NADP^+$ from $^2D_4$-nicotinamide.

(**H**) Normalized peak areas for newly synthesized NAD^+ [M+3] and $NADP^+$ [M+3] from NADK-deficient HEK-293 cells expressing either empty vector (EV) or the indicated NADK variants (WT, ∆1-37, ∆1-68, ∆1-87, ∆81-90, and ISO3) following 2h labeling with 2,4,5,6-^{2}D-nicotinamide. Data are shown as the mean ± S.E.M. of biological triplicates. The data is representative of at least two independent experiments. ****$p < 0.001$ was calculated with one-way ANOVA.

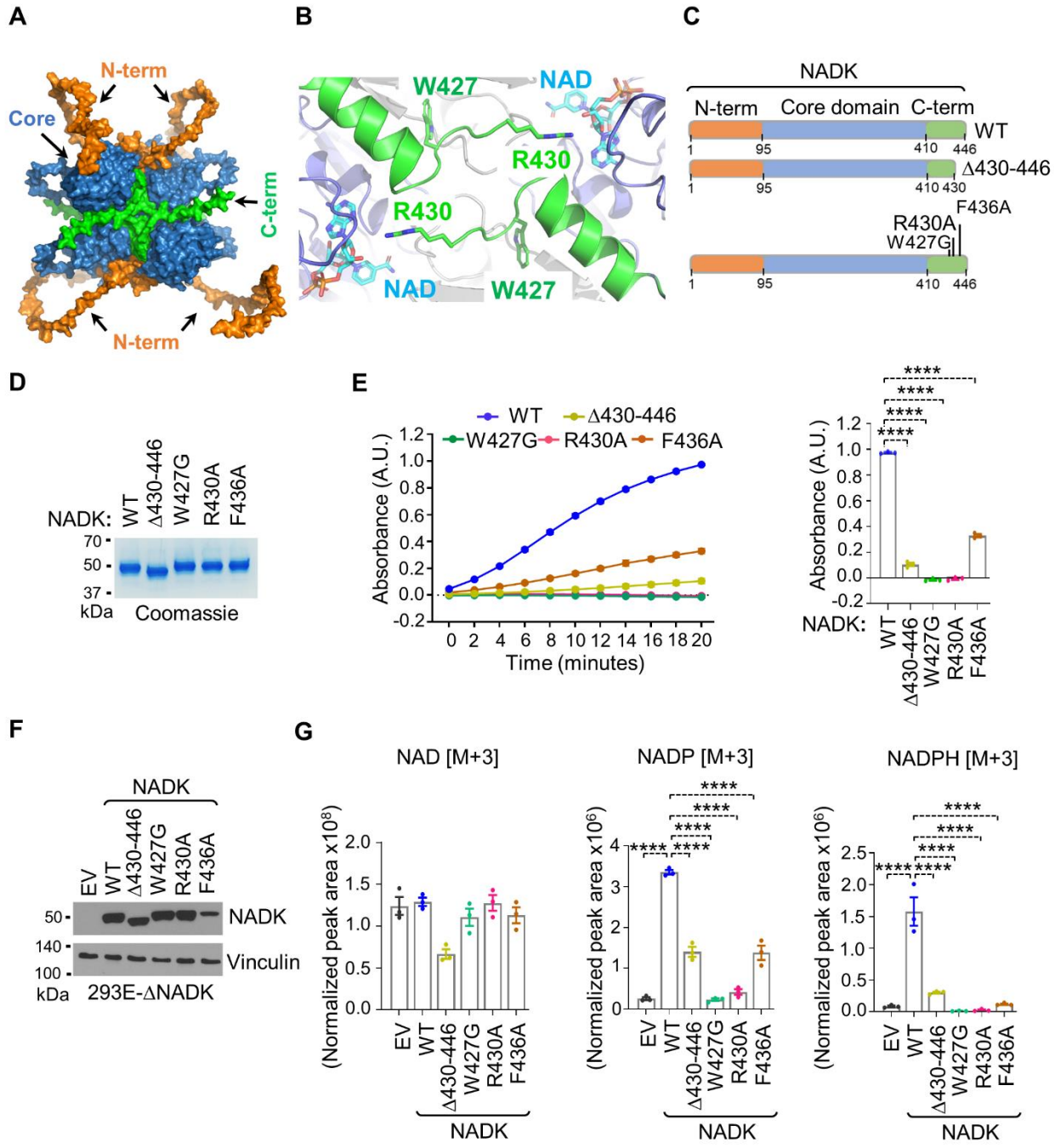
A
N-term
Core
C-term
N-term
B
W427
NAD
R430
R430
NAD
W427
C
NADK
N-term
Core domain
C-term
WT
1
95
410
446
Δ430-446
1
95
410
430
F436A
R430A
W427G
1
95
410
446
D
NADK:
WT
Δ430-446
W427G
R430A
F436A
70
50
37
kDa
Coomassie
E
WT
Δ430-446
W427G
R430A
F436A
Absorbance (A.U.)
Time (minutes)
Absorbance (A.U.)
NADK:
WT
Δ430-446
W427G
R430A
F436A
F
NADK
EV
WT
Δ430-446
W427G
R430A
F436A
50
140
100
kDa
NADK
Vinculin
293E-ΔNADK
G
NAD [M+3]
NADP [M+3]
NADPH [M+3]
(Normalized peak area x10^8)
(Normalized peak area x10^6)
(Normalized peak area x10^6)
EV
WT
Δ430-446
W427G
R430A
F436A
NADK

Fig. 4. The C-terminus is essential for maintaining NADK activity.

(**A**) AlphaFold model of wild-type hsNADK as a tetramer. N-tail, catalytic core and C-tail of hsNADK are shown in orange, blue and green, respectively.

(**B**) Zoom in the cryo-EM structure of $hsNADK_{esv}$. The very C-terminal helix (residues 413-424) of the catalytic core and the start of the C-tail (residues 427-430) are shown in green ribbon. The NAD^+ binding site is highlighted with the NAD^+ molecules drawn in stick. The side-chains of W427 and R430 are also shown as stick. Figure drawn using PyMOL as (A).

(**C**) Schematics of NADK (full length) and different C-terminus variants, including Δ430-446, W427G, R430A, and F436A, are color-coded as follows: N-terminus domain (orange), the kinase domain (blue), and C-terminus (green).

(**D**) Coomassie blue staining of the indicated purified NADK C-terminal variants from HEK-293 cells.

(**E**) *In vitro* enzymatic activity assay for the indicated immunopurified NADK variants (WT, Δ430-446, W427G, R430A, and F436A). Bar graphs show A340 values after 20 min of the reaction. The absorbance values are shown as the mean ± S.E.M. of biological triplicates. The data is representative of three independent experiments.

(**F**) Immunoblotting from NADK-deficient HEK-293 cells expressing either empty vector (EV) or the indicated NADK variants (WT, Δ430-446, W427G, R430A, and F436A).

(**G**) Normalized peak areas for newly synthesized NAD^+ [M+3], $NADP^+$ [M+3], and NADPH [M+3], from NADK-deficient HEK-293 cells expressing either empty vector (EV) or the indicated NADK $NADP^+$ [M+3], following 2h labeling with 2,4,5,6-^{2}D-nicotinamide. Data are shown as the mean ± S.E.M. of biological triplicates. The data is representative of at least two independent experiments. ****$p < 0.001$ was calculated with one-way ANOVA.

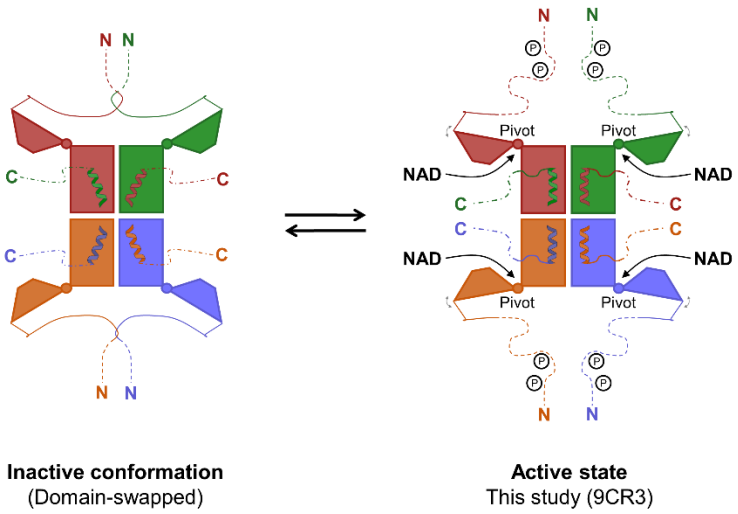

Figure 5: Schematic model illustrating the regulation of hsNADK by its terminal regions. In hsNADK, intertwined pairs of N-terminal tails lock the catalytic domains in an inactive conformation, preventing the proper orientation of the C-terminal helix and the folding of the C-terminal tail over the active site. Post-translational modifications, such as phosphorylation, may trigger the separation of the N-tails, enabling the hinge motion of the N-terminal domain to accommodate NAD. Concurrently, the C-terminal helix readjusts to anchor the C-tail, forming a fully functional active site.

Table 1. CryoEM data collection and refinement statistics.

	$hsNADK_{FL}$ (EMD-45831) (PDB: 9CR3)	$NADK_{esv}$ (EMD-45832) (PDB: 9CR4)	$NADK_{esv}$ -NAD (EMD-45856) (PDB: 9CRA)
Data collection and processing			
Microscope	Titan Krios		
Nominal magnification	105,000	105,000	165,000
Voltage (kV)	300		
Electron exposure ($e^-/Å^{-2}$)	50		
Defocus range (μm)	-0.9 to -2.2		
Pixel size (Å)	0.83	0.834	0.738
Symmetry imposed	D2		
Initial particle images (no.)	1,820,219	4,587,353	1,716,164
Final particle images (no.)	77,606	316,306	251,813
Map resolution (Å)	3.18	2.81	2.34
FSC threshold	0.143		
Map pixel size (Å)	0.83	1.043	1.046
Refinement			
Initial model used	ab initio		
Model composition			
Nonhydrogen atoms	9,299	9,099	9,842
Number of Protein residues	1,200	1,179	1,247
Number of Ligands	0	0	4
R.m.s. deviations			
Bond lengths (Å)	0.003	0.003	0.003
Bond angles (˚)	0.620	0.560	0.606
Validation			
MolProbity score	1.94	1.89	2.01
Clashscore	10.49	7.48	10.51
Poor rotamers (%)	0	0	0
Ramachandran plot			

Favored (%)	94.0	92.3	92.4
Allowed (%)	6.0	7.7	7.6
Disallowed (%)	0	0	0

Science Advances
AAAS

Supplementary Materials for

Cryo-EM structure and regulation of human NAD kinase

Prakash P. Praharaj *et al.*

*Corresponding author:

Gilles Labesse, labesse@cbs.cnrs.fr; Gerta Hoxhaj, gerta.hoxhaj@utsouthwestern.edu

This PDF file includes:

Table S1. Post-translational modifications of NADK expressed in HEK-293 cells.

Site	Peptide Sequence	Phospho-Peptide modifications	Abundance of modification (10^6)	Total peptide abundance (10^6)	% modified peptide	Phosphosite®
S15	MTMNKESPDAAAYCCSACHGDETWSYNHPIR	1xPhospho [S8]	23.431	181.948	12.88	3HTP
S15	ELSPDAAAYCCSACHGDETWSYNHPIR	1xPhospho [S3]	350.63	6896.52	5.08	3HTP
S15	ELSPDAAAYCCSACHGDETWSYNHPIRGR	1xPhospho [S3]	37.426	1849.1	2.02	3HTP
S15, S24	ELSPDAAAYCCSACHGDETWSYNHPIR	2xPhospho [S3; S12]	0.184	6896.52	0.0027	
S44	AKSRSLSASPALGSTK	1xPhospho [S3]	ND	2.097		10HTP
S46	SRSLSASPALGSTKEFR	1xPhospho [S3]	0.537	0.537	100	30HTP
S46	SRSLSASPALGSTK	1xPhospho [S3]	80.528	429.29	18.76	30HTP
S44, S46	AKSRSLSASPALGSTK	2xPhospho [S3; S5]	2.097	2.097	100	
S48	SLSASPALGSTKEFRR	1xPhospho [S3]	3.161	93.74	3.37	37HTP
S46; S48	SRSLSASPALGSTK	2xPhospho [S3; S5]	103.22	429.29	24.04	
S48; S50	SLSASPALGSTK	2xPhospho [S3; S5]	64.916	12857.7	0.5	
S46; S48; S50	SRSLSASPALGSTK	3xPhospho [S3; S5; S7]	ND	429.29		
S64	TRSLHGPCPVTTFGPKACVLQNPQTIMHIQDPASQR	1xPhospho [S3]	0.94	5.224	17.99	44HTP
S64	TRSLHGPCPVTTFGPK	1xPhospho [S3]	550.51	554.56	99.27	44HTP
S64	SLHGPCPVTTFGPK	1xPhospho [S1]	145.59	20746	0.702	44HTP
T62; S64; T/S	TRSLHGPCPVTTFGPKACVLQNPQTIMHIQDPASQR	3xPhospho [T1; S3; T/S]	0.96	5.224	18.378	
S117	MRDASLLQPFK	1xPhospho [S5]	29.61	2227.72	1.33	

S117	DASLLQPFK	1xPhospho [S3]	49.97	18432.1	0.27	
S117	DASLLQPFKELCTHLMEENMIVYVEK	1xPhospho [S3]	2.64	869.8	0.3	
S153	KVLEDPAIASDESFGAVK	1xPhospho [S13]	ND	5316.8		
S153	VLEDPAIASDESFGAVK	1xPhospho [S12]	ND	23471.5		
S371	IMLSPEAR	1xPhospho [S4]	10.15	21843.4	0.05	
S395	HGDSISITTSCYPLPSICVR	1xPhospho [S4]	2.0	5930.09	0.03	
Site	**Peptide Sequence**	**Methylation events**	**Abundance of modification (10^6)**	**Total peptide abundance (10^6)**	**% modified peptide**	**Phosphosite®**
K12	MTMNKELSPDAAAYCCSACHGDETWSYNHPIR	1xTrimethyl [K5]	77.5	181.948	42.59	
K12	MTMNKELSPDAAAYCCSACHGDETWSYNHPIR	1xDimethyl [K5]	ND	181.948		
K12, T9	MTMNKELSPDAAAYCCSACHGDETWSYNHPIR	1xDimethyl [K5]; 1xPhospho [T2]	ND	181.948		
R39	ELSPDAAAYCCSACHGDETWSYNHPIRGRAK	1xDimethyl [R27]	4.52	4.52	100	3HTP
R41	ELSPDAAAYCCSACHGDETWSYNHPIRGRAK	1xTrimethyl [R29]	1.74	1.74	100	5HTP
K43	AKSRSLSASPALGSTK	1xTrimethyl [K2]	ND	2.097		
R45	AKSRSLSASPALGSTK	1xDimethyl [R4]	ND	2.097		
R45	SRSLSASPALGSTK	1xMethyl [R2]	182.34	429.29	42.48	1HTP
R45	SRSLSASPALGSTK	1xDimethyl [R2]	44.709	429.29	10.41	1HTP
K57	SLSASPALGSTKEFR	1xMethyl [K12]	1.176	12857.7	0.01	
K77	TRSLHGPCPVTTFGPKACVLQNPQTIMHIQDPASQR	1xTrimethyl [K16]; 1xPhospho [T/S]	ND	5.224		

K77	SLHGPCPVTTFGPKACVLQNPQTIMHIQD-PASQR	1xDimethyl [K14]	17.75	408.04	4.35	
K77	SLHGPCPVTTFGPKACVLQNPQTIMHIQD-PASQR	1xTrimethyl [K14]	93.71	408.04	22.97	
R97	ACVLQNPQTIMHIQDPASQR	1xDimethyl [R20]	ND	26137.2		
K123	DASLLQPFKELCTHLMEENMIVYVEK	1xTrimethyl [K9]	ND	869.8		
K140	ELCTHLMEENMIVYVEK	1xDimethyl [K17]	ND	15711.6		
K141	KVLEDPAIASDESFGAVK	1xMethyl [K1]	116.68	5316.8	2.19	
K141	KVLEDPAIASDESFGAVK	1xTrimethyl [K1]	2.245	5316.8	0.04	
K141	KVLEDPAIASDESFGAVKK	1xMethyl [K1]	4.53	743.82	0.61	
K141	KVLEDPAIASDESFGAVKK	1xDimethyl [K1]	ND	743.82		
K158	VLEDPAIASDESFGAVK	1xMethyl [K17]	121.53	23471.5	0.52	
K158	VLEDPAIASDESFGAVKK	1xTrimethyl [K17]	5.74	3100.82	0.19	
K158	VLEDPAIASDESFGAVKK	1xMethyl [K17]	6.39	3100.82	0.21	
K158; K159; K160	KVLEDPAIASDESFGAVKKK	3xMethyl [K18; K19; K20]	ND	6.16		
R290	QAMQYQVLNEVVIDR	1xMethyl [R15]	4.69	8198.9	0.06	
Site	**Peptide Sequence**	**Acetylation events**	**Abundance of modification (10^6)**	**Total peptide abundance (10^6)**	**% modified peptide**	**Phosphosite®**
K12	MTMNKESPDAAAYCCSACHGDETWSYN-HPIR	1xAcetyl [K5]	79.445	181.948	43.66	
K43	AKSRSLSASPALGSTK	1xAcetyl [K2]	ND	2.097		
K57	SLSASPALGSTK	1xAcetyl [K12]	9.69	12857.7	0.08	2HTP
K77	SLHGPCPVTTFGPKACVLQNPQTIMHIQD-PASQR	1xAcetyl [K14]	61.67	408.04	15.11	
T62; K77	TRSLHGPCPVTTFGPKACVLQNPQTIM-HIQDPASQR	1xPhospho [T1]; 1xAcetyl [K16]	3.324	5.224	63.623	

S64; K77	TRSLHGPCPVTTFGPKACVLQNPQTIM-HIQDPASQR	1xPhospho [S3]; 1xAcetyl [K16]	ND	5.224		
K102	LTWNKSPK	1xAcetyl [K5]	42.51	154.7	27.48	
K105	SPKSVLVIK	1xAcetyl [K3]	71.54	191.56	37.35	
K111	SVLVIKK	1xAcetyl [K6]	64.42	64.42	100	
K140	ELCTHLMEENMIVYVEKK	1xAcetyl [K17]	6.64	259.07	2.56	
K141	KVLEDPAIASDESFGAVK	1xAcetyl [K1]	20.94	5316.8	0.39	
K158	KVLEDPAIASDESFGAVKK	1xAcetyl [K18]	14.35	743.82	1.93	1HTP
K158	VLEDPAIASDESFGAVK	1xAcetyl [K17]	3.79	23471.5	0.02	1HTP
K158	VLEDPAIASDESFGAVKK	1xAcetyl [K17]	27.38	3100.82	0.88	1HTP
K158	VLEDPAIASDESFGAVKK	1xMethyl [K17]	6.39	3100.82	0.21	1HTP

A

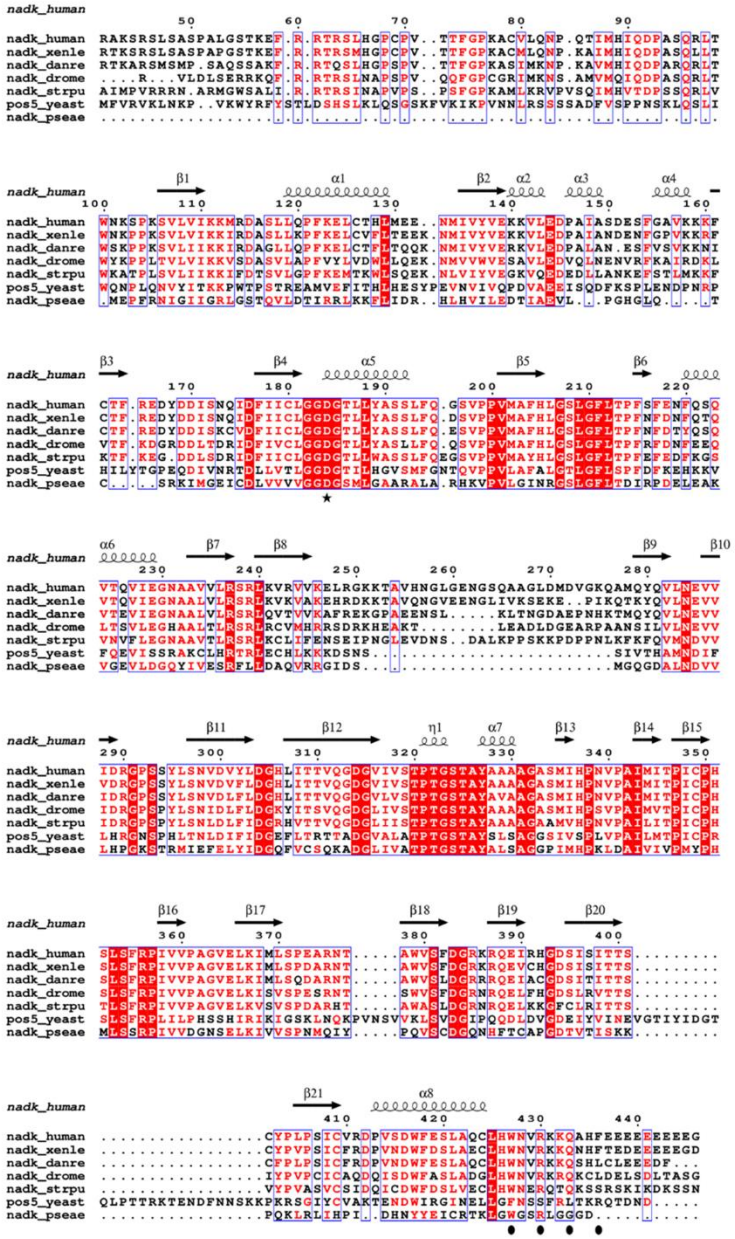
nadk_human
nadk_xenle
nadk_danre
nadk_drome
nadk_strpu
pos5_yeast
nadk_pseae

B

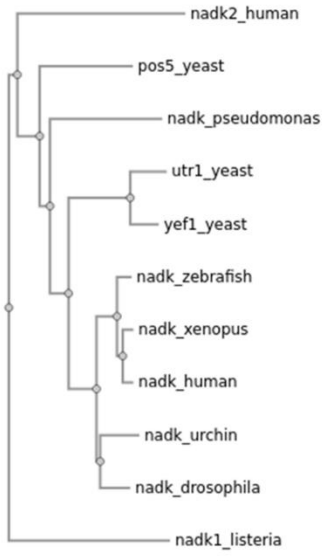
nadk2_human
pos5_yeast
nadk_pseudomonas
utr1_yeast
yef1_yeast
nadk_zebrafish
nadk_xenopus
nadk_human
nadk_urchin
nadk_drosophila
nadk1_listeria

Fig. S1. Comparative Sequence Alignment and Phylogenetic Analysis of NADKs.

(**A**) Sequence alignment of NADKs. A multiple sequence alignment shown of cytosolic NADKs from representative animals (human: nadk_human, Xenopus: nadk_xenle, zebrafish: nadk_danre, drosophila: nadk_drome and see urchin: nadk_strpu), alongside the mitochondrial NADK from yeast (pos5_yeast) and from a bacterial pathogen, *Pseudomonas aeruginosa* (nadk_pseae). The catalytic aspartate is highlighted with a black star, and the functionally important residues from the C-tail (this study) are shown in black circle. The figure was generated using Espript (https://espript.ibcp.fr/ESPript/ESPript/).

(**B**) Evolution of NADKs. A phylogenic tree of various NADKs was built using the software Ibis2Analyzer (http://ibis2analyzer.lcqb.upmc.fr/). Cytosolic NADKs from animals appear more closely related to those NADKs from gram (-) bacteria, than the human mitochondrial NADK2 (nadk2_human).

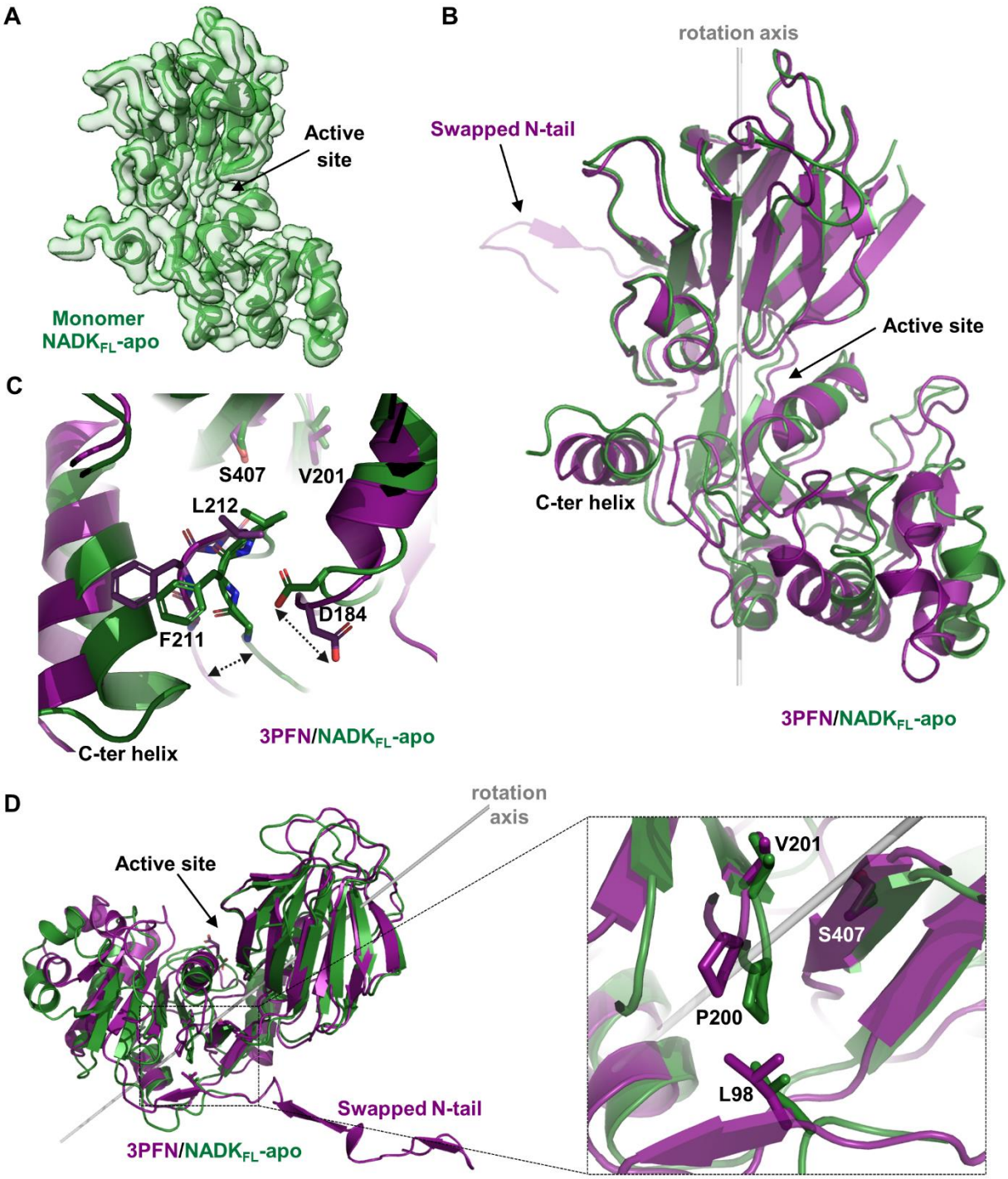
A
Active site
Monomer NADK$_{FL}$-apo
B
rotation axis
Swapped N-tail
Active site
C-ter helix
3PFN/NADK$_{FL}$-apo
C
S407
V201
L212
D184
F211
C-ter helix
3PFN/NADK$_{FL}$-apo
D
rotation axis
Active site
Swapped N-tail
3PFN/NADK$_{FL}$-apo
V201
S407
P200
L98

Figure S2: Comparative analysis of the cryo-EM full-length $NADK_{FL}$ and crystal structure of a truncated hsNADK

(**A**) Electron density and molecular model of a monomer of apo $NADK_{FL}$.

(**B**) Comparison of apo $NADK_{FL}$ cryo-EM monomer in green and that of the crystal structure of a truncated construct of hsNADK (PDB3PFN; unpublished) in violet. The main rotation axis is shown in light grey.

(**C**) Comparison of the active sites of apo $NADK_{FL}$ and the crystal structure 3PFN. Zoom of the core of the catalytic domains showing the positions of the two pivots, namely V201 and S407, and two highly conserved residues, F211 and L212. The re-orientation of the catalytic aspartate D184 and its interactions with the backbone nitrogens of F211 and L212 are shown. Same color code as in (B).

(**D**) Interaction network connecting the N-tail (especially L98) and the hinge pivots (V201 and S407) through proline P200 in hsNADK (3PFN) and the $NADK_{FL}$ cryo-EM structure (color code as in B). Panels B-D were drawn using PyMOL.

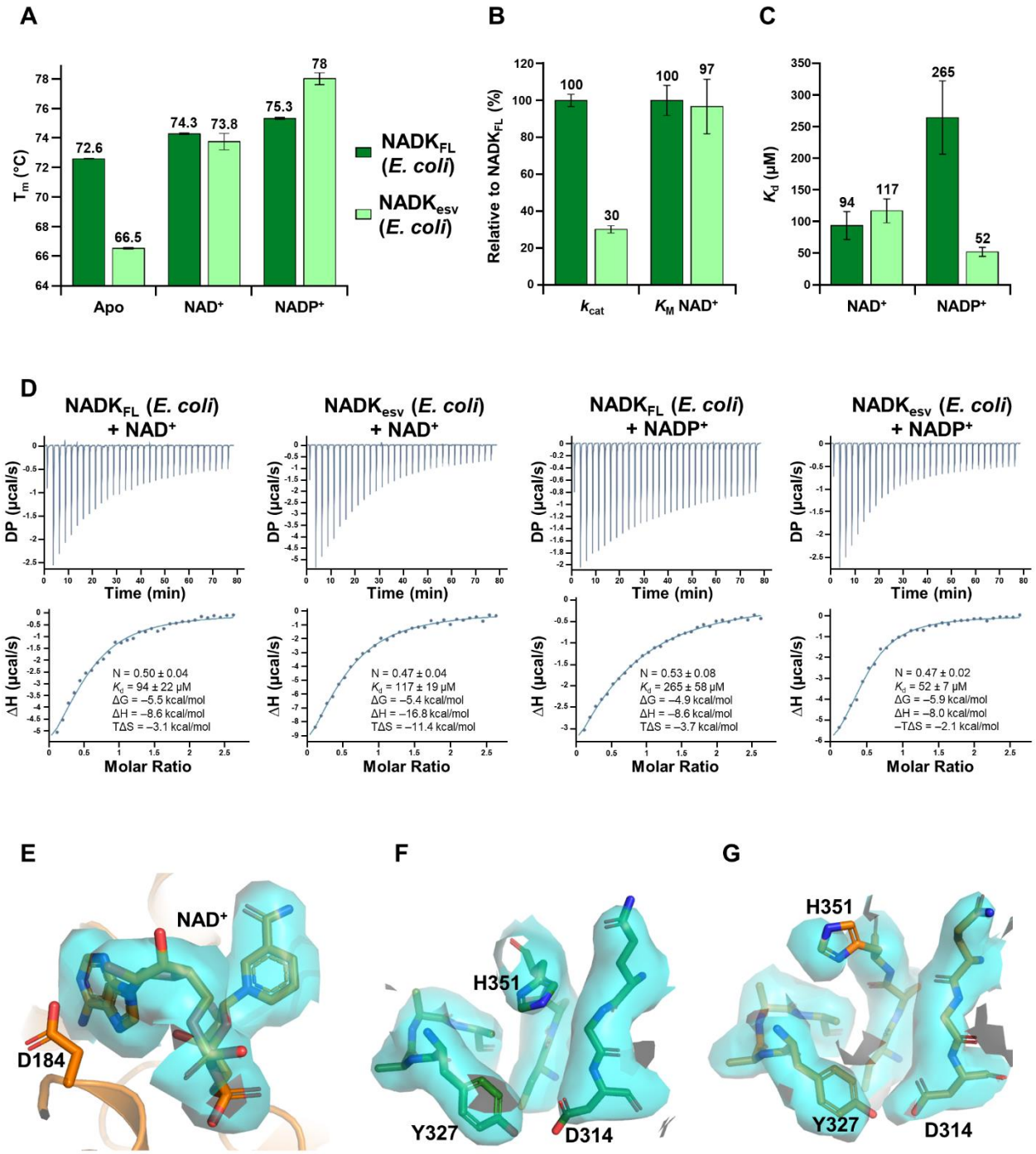
A
B
C
D
E
F
G
T_m (°C)
72.6
66.5
74.3
73.8
75.3
78
Apo
NAD+
NADP+
NADK$_{FL}$ (*E. coli*)
NADK$_{esv}$ (*E. coli*)
Relative to NADK$_{FL}$ (%)
100
30
100
97
k_{cat}
K_M NAD+
K_d (µM)
94
117
265
52
NADK$_{FL}$ (*E. coli*) + NAD+
NADK$_{esv}$ (*E. coli*) + NAD+
NADK$_{FL}$ (*E. coli*) + NADP+
NADK$_{esv}$ (*E. coli*) + NADP+
DP (µcal/s)
Time (min)
ΔH (µcal/s)
Molar Ratio
N = 0.50 ± 0.04
K_d = 94 ± 22 µM
ΔG = –5.5 kcal/mol
ΔH = –8.6 kcal/mol
TΔS = –3.1 kcal/mol
N = 0.47 ± 0.04
K_d = 117 ± 19 µM
ΔG = –5.4 kcal/mol
ΔH = –16.8 kcal/mol
TΔS = –11.4 kcal/mol
N = 0.53 ± 0.08
K_d = 265 ± 58 µM
ΔG = –4.9 kcal/mol
ΔH = –8.6 kcal/mol
TΔS = –3.7 kcal/mol
N = 0.47 ± 0.02
K_d = 52 ± 7 µM
ΔG = –5.9 kcal/mol
ΔH = –8.0 kcal/mol
–TΔS = –2.1 kcal/mol
NAD+
D184
H351
Y327
D314
H351
Y327
D314

Figure S3: Biochemical Characterization of hsNADK

(**A**) Thermal stability of $NADK_{FL}$ (dark green) and $NADK_{esv}$ (light green) in its apo form and in complex with NAD^+ or $NADP^+$.

(**B**) Relative kinetic parameters, steady state rate constant and Michaelis constant for NAD^+, of $NADK_{esv}$ compared to $NADK_{FL}$ (color code as in A).

(**C**) Dissociation constants of NAD^+ or $NADP^+$ from $NADK_{FL}$ and $NADK_{esv}$ (color code as in A).

(**D**) ITC isotherms for the binding of NAD^+ and $NADP^+$ to $NADK_{FL}$ or $NADK_{esv}$ are shown. Values deduced from the isotherms are displayed under each curve.

(E) Electron density of the NAD^+ molecule. The electron density for the NAD^+ molecule bound to $NADK_{esv}$ is shown in cyan surface. The ligand and the side chain of D184 are shown in sticks.

(**F**) Electron density and model of the active site around histidine H351 in the apo-form of $NADK_{FL}$. The electron density is shown in cyan surface, and protein residues are shown in dark green sticks.

(G) Electron density and model of the active site around histidine H351 in the NAD^+-bound form of $NADK_{esv}$. The electron density is shown in cyan surface, and protein residues are shown in orange sticks.

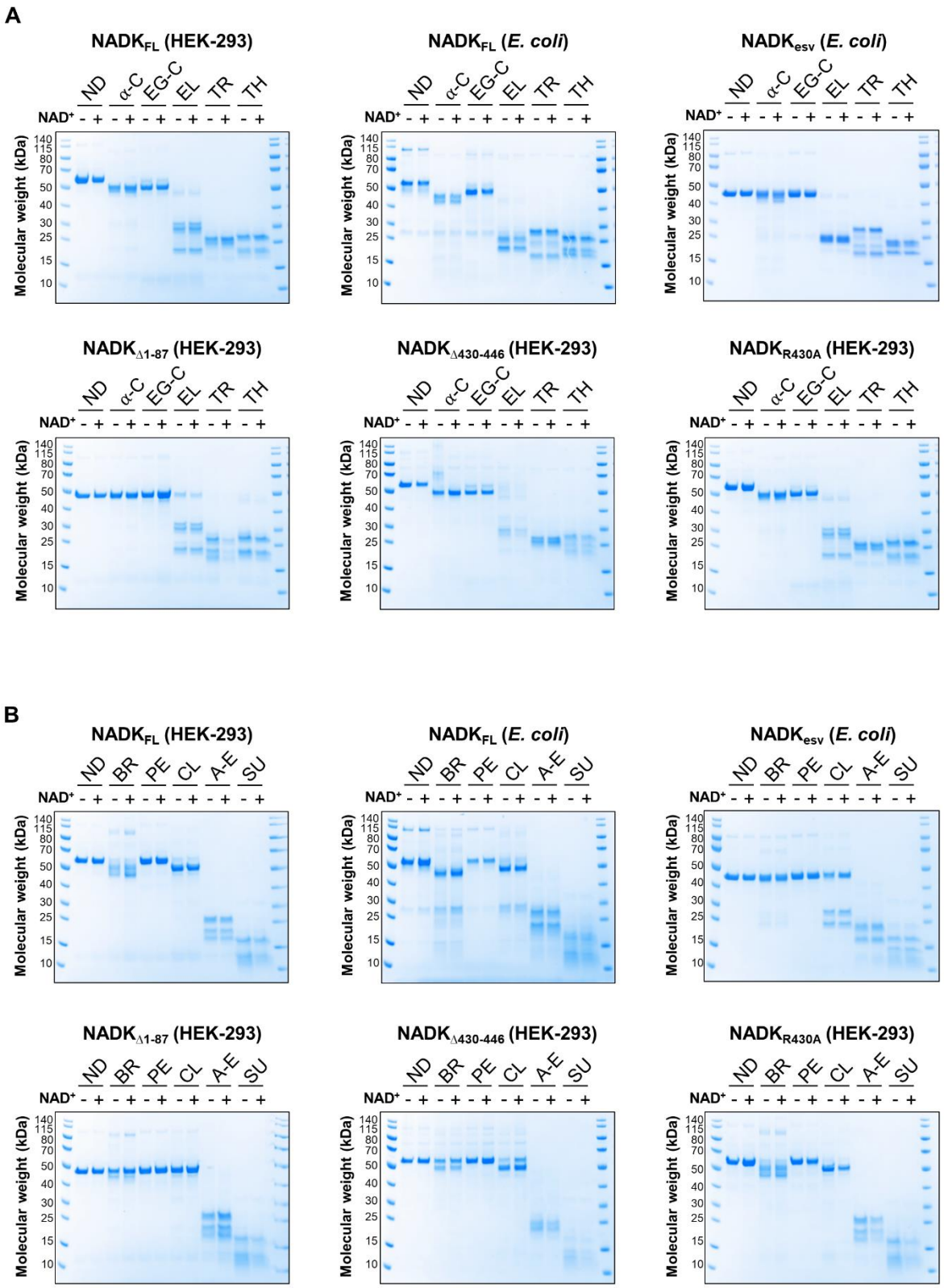
A
NADK$_{FL}$ (HEK-293)
NADK$_{FL}$ (*E. coli*)
NADK$_{esv}$ (*E. coli*)
NADK$_{\Delta 1\text{-}87}$ (HEK-293)
NADK$_{\Delta 430\text{-}446}$ (HEK-293)
NADK$_{R430A}$ (HEK-293)
ND α-C EG-C EL TR TH
NAD+ - + - + - + - + - + - +
Molecular weight (kDa)
140 115 80 70 50 40 30 25 15 10
B
NADK$_{FL}$ (HEK-293)
NADK$_{FL}$ (*E. coli*)
NADK$_{esv}$ (*E. coli*)
NADK$_{\Delta 1\text{-}87}$ (HEK-293)
NADK$_{\Delta 430\text{-}446}$ (HEK-293)
NADK$_{R430A}$ (HEK-293)
ND BR PE CL A-E SU
NAD+ - + - + - + - + - + - +
Molecular weight (kDa)
140 115 80 70 50 40 30 25 15 10

Figure S4: Proteolysis profiles of various hsNADK constructs.

(**A, B**) A panel of diluted proteases was used to partially digest (1 hour) different hsNADK constructs (purified from mammalian cells or bacteria), followed by analysis with SDS-PAGE gels. Constructs labeled as described in the text: $NADK_{FL}$ (HEK-293), $NADK_{FL}$ (E. coli), $NADK_{esv}$ (*E. coli*), NADK $_{\Delta 1\text{-}87}$ (HEK-293), $NADK_{\Delta 430\text{-}446}$ (HEK-293), and $NADK_{R430A}$ (HEK-293) were treated with the indicated proteases.

(**A**) Proteases used include ND = Not Digested, α-C = α-Chymotrypsin, EG-C = Endoproteinase Glu-C, EL = Elastase, TR = Trypsin, TH = Thermolysin.

(**B**) Proteases used include: ND = Not Digested, Br = Bromelain, PE = Pepsin, CL = Clostripain, A-E = Actinase-E, SU = Subtilisin.

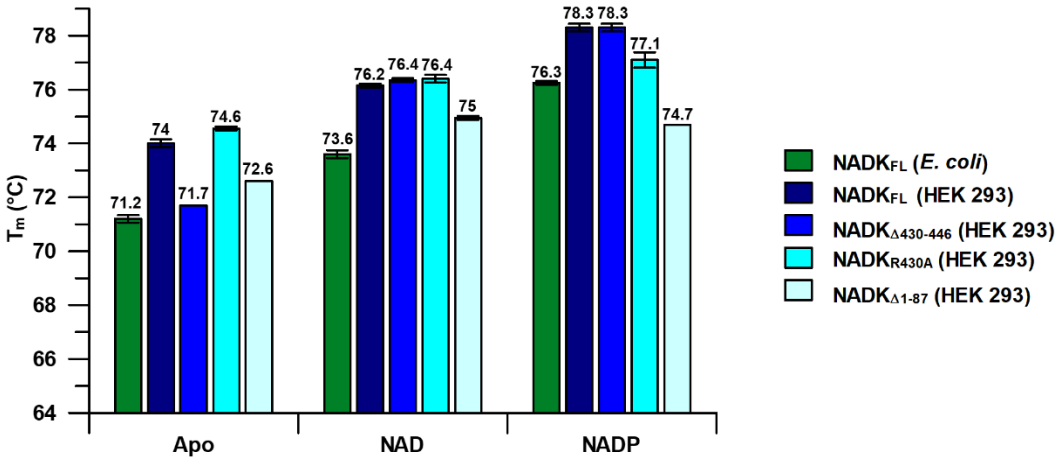

Figure S5: Thermal stability of various hsNADK constructs.

The thermostability of $NADK_{FL}$ purified from bacteria (dark green) and HEK-293 cells (dark blue) is compared with that of several hs$NADK_{FL}$ mutants purified from HEK-293 cells, both in the absence and presence of ligands (NAD^+ or $NADP^+$).

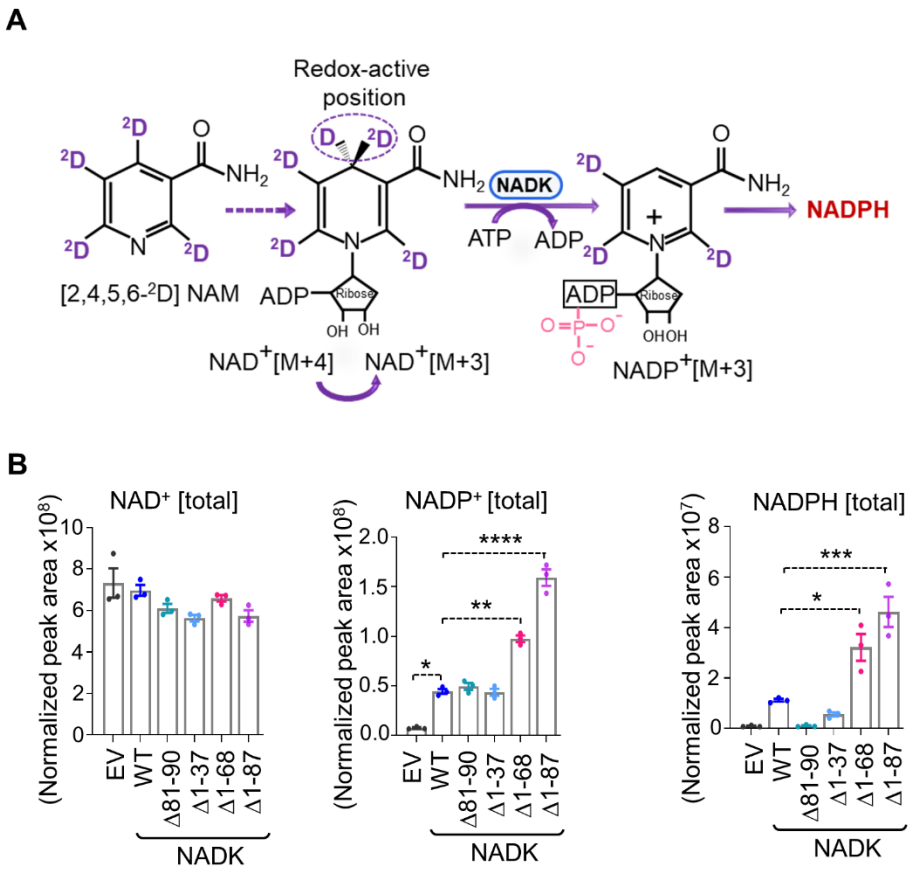

Fig. S6. Impact of the N-terminal deletions on cellular NAD(P)(H) pools.

(**A**) Schematics of labeling of NAD^+ and $NADP^+$ from $^2D_4$-nicotinamide. Redox-active positions are indicated.

(**B**) Normalized peak areas showing total NAD^+, $NADP^+$ and NADPH pools from NADK-deficient HEK293 cells expressing either empty vector (EV) or the indicated NADK variants (WT, Δ1-37, Δ1-68, Δ1-87, Δ81-90, and ISO3). All the data are shown as the mean ± S.E.M. of biological triplicates from at least two independent experiments. $*p < 0.05$, $**p < 0.01$, $***p < 0.001$, $****p < 0.0001$ were calculated with one-way ANOVA and Sidak Post-hoc test.

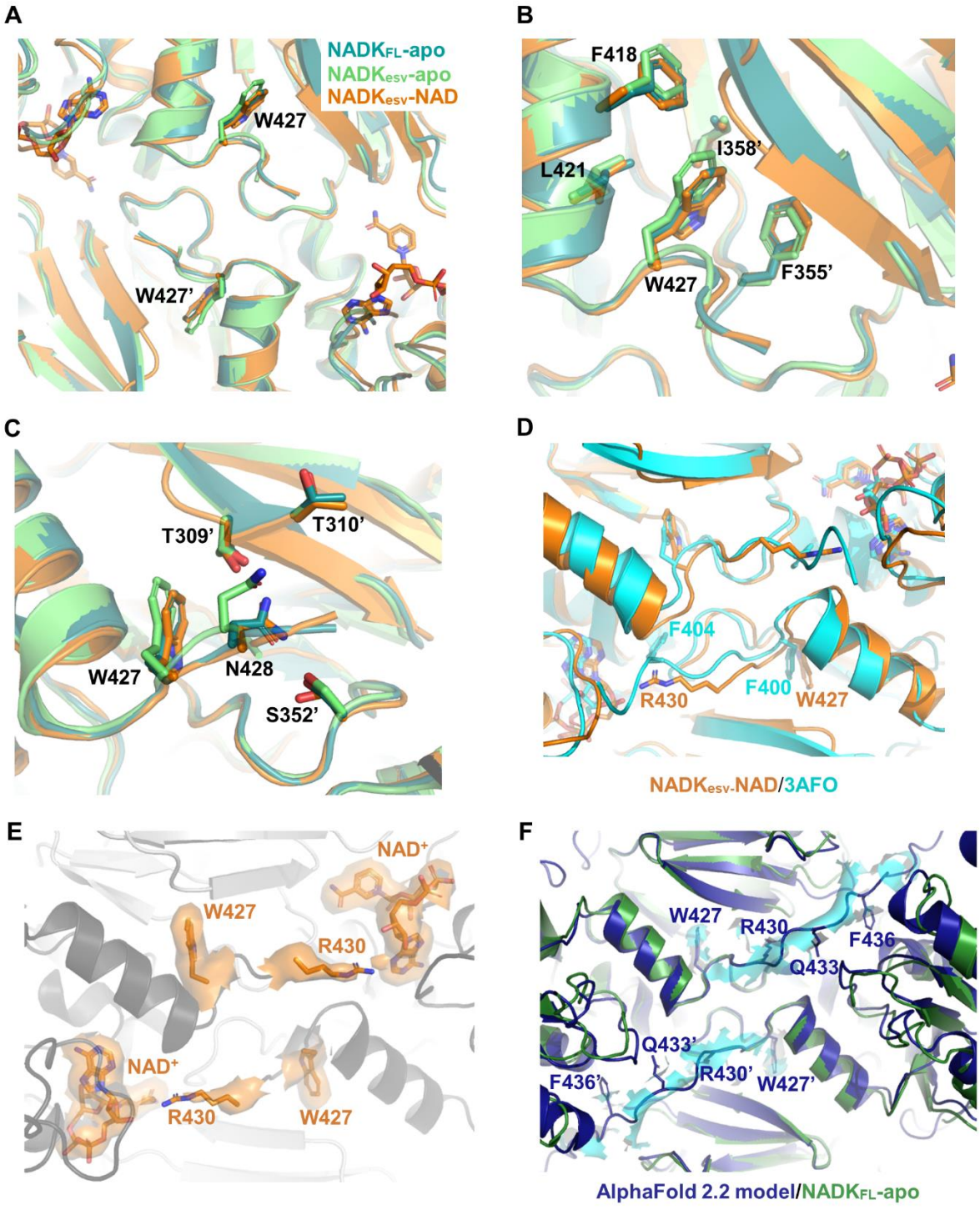
A
NADKFL-apo
NADKesv-apo
NADKesv-NAD
W427
W427'
B
F418
I358'
L421
W427
F355'
C
T309'
T310'
W427
N428
S352'
D
F404
R430
F400
W427
NADKesv-NAD/3AFO
E
NAD+
W427
R430
NAD+
R430
W427
F
W427
R430
F436
Q433
Q433'
F436'
R430'
W427'
AlphaFold 2.2 model/NADKFL-apo

Figure S7. Structural analysis of the C-terminal tail of NADK

(**A**) Zoom in the C-terminal region of the hsNADK. Comparison of the three cryo-EM structure hsNADK$_{FL}$-apo (teal), hsNADK$_{esv}$-apo (green), and hsNADK$_{esv}$-NAD$^+$ (orange). These structures highlight the positioning of a conserved and functionally important tryptophan W427 relative to the binding site of NAD$^+$.

(**B**) Zoom in the cryo-EM structures of hsNADK. Side-chains of hydrophobic residues (F418, L421 from one monomer and F355' and I358' from a second monomer) in contact with the tryptophan W427 are shown in stick, while the remaining of the structure is shown as ribbons.

(**C**) Zoom in the cryo-EM structures of hsNADK. Side-chains of the conserved asparagine N428 (following W427) and those of the interacting residues (S309', T310' and F355' from a second monomer) are shown in stick, while the remaining of the structure is shown as ribbons.

(**D**) Comparison of the C-termini of hsNADK and yeast POS5 (PDB3AFO). The NAD$^+$-bound structure of hsNADK$_{esv}$ and the NAD$^+$-bound form of POS5 are shown in orange and cyan, respectively. The tryptophan W427 and arginine R430 and the equivalent residues in yeast POS5 (F400 and F404) are shown in stick.

(**E**) Zoom in the region of the C-tail of hsNADK, highlighting the positions of the bound NAD$^+$ molecules and conserved functionally important residues (W427, R430) that are visible in the cryoEM structures of hsNADK. The protein is shown as grey ribbons while the NAD$^+$ and the side-chains of W427 and R430 are shown in orange sticks. The electron density from hsNADK$_{esv}$-NAD is shown in orange surface.

(**F**) Hybrid model of C-tail of hsNADK. Zoom in the region of C-tail of hsNADK highlights the positions of conserved functionally important residues (W427, R430, Q433, and F436). The C-tail predicted by Alphafold was slightly reoriented to fit into the residual density of hsNADK$_{FL}$-apo. The C-terminal helix and tail are shown in dark-green ribbons, while the hybrid model is in blue ribbons. The extra electron density from hsNADK$_{FL}$-apo is shown in cyan surface. Panels A-F are drawn using PyMOL.

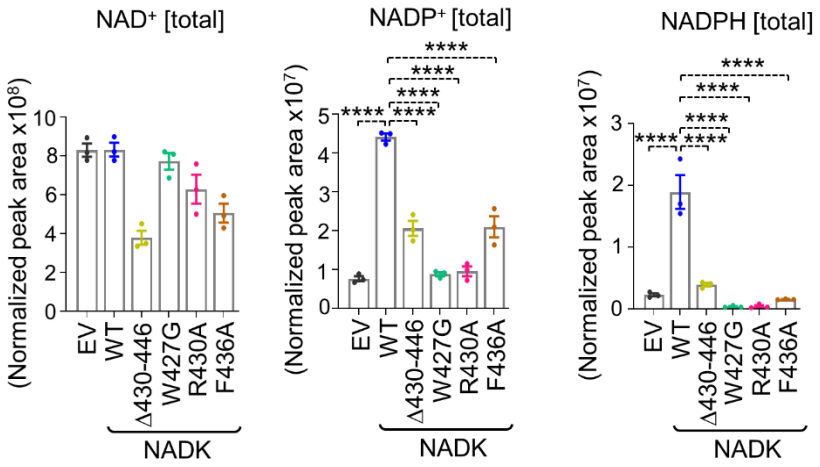

Fig. S8. Effects of the C-terminal NADK mutations on cellular NAD(P)(H) pools.

Normalized peak areas showing total NAD^+, $NADP^+$, and NADPH pools from NADK-deficient HEK293 cells expressing either empty vector (EV) or the indicated NADK variants (WT, Δ430-446, W427G, R430A, and F436A). All the data are shown as the mean ± S.E.M. of biological triplicates from at least two independent experiments. ****$p < 0.0001$ was calculated with one-way ANOVA and Sidak Post-hoc test.

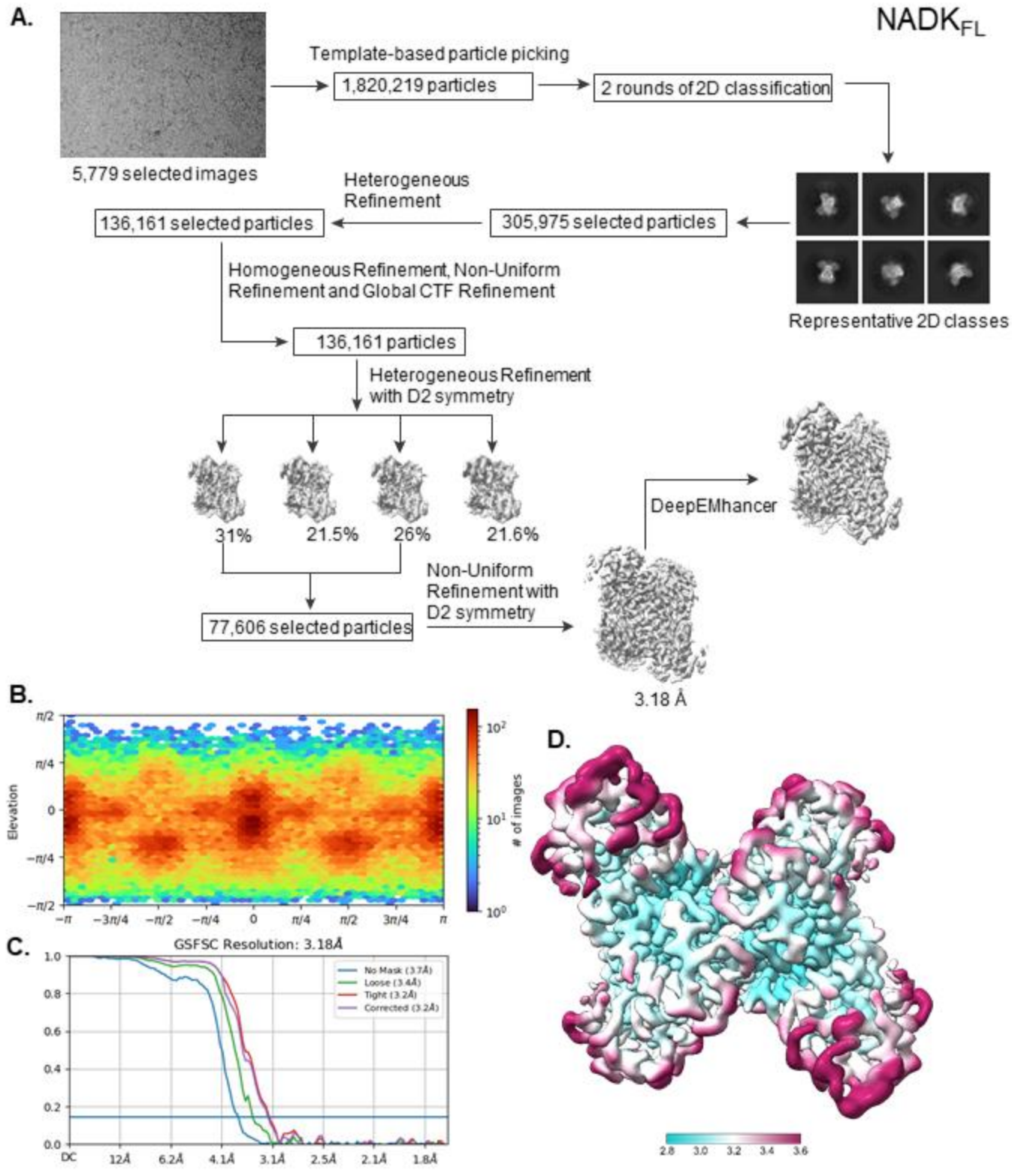
A.
NADK$_{FL}$
Template-based particle picking
1,820,219 particles
2 rounds of 2D classification
5,779 selected images
Representative 2D classes
Heterogeneous Refinement
136,161 selected particles
305,975 selected particles
Homogeneous Refinement, Non-Uniform Refinement and Global CTF Refinement
136,161 particles
Heterogeneous Refinement with D2 symmetry
31%
21.5%
26%
21.6%
DeepEMhancer
Non-Uniform Refinement with D2 symmetry
77,606 selected particles
3.18 Å
B.
Elevation
# of images
C.
GSFSC Resolution: 3.18Å
No Mask (3.7Å)
Loose (3.4Å)
Tight (3.2Å)
Corrected (3.2Å)
D.

Figure S9: Cryo-EM Image Processing for $NADK_{FL}$.

(**A**) Flowchart of the cryo-EM data processing of $NADK_{FL}$.

(**B**) The Euler angle distribution plot from cryoSPARC.

(**C**) The gold-standard Fourier shell correlation (GS-FSC) curves from cryoSPARC.

(**D**) Local resolution estimation of the cryo-EM map of $NADK_{FL}$.

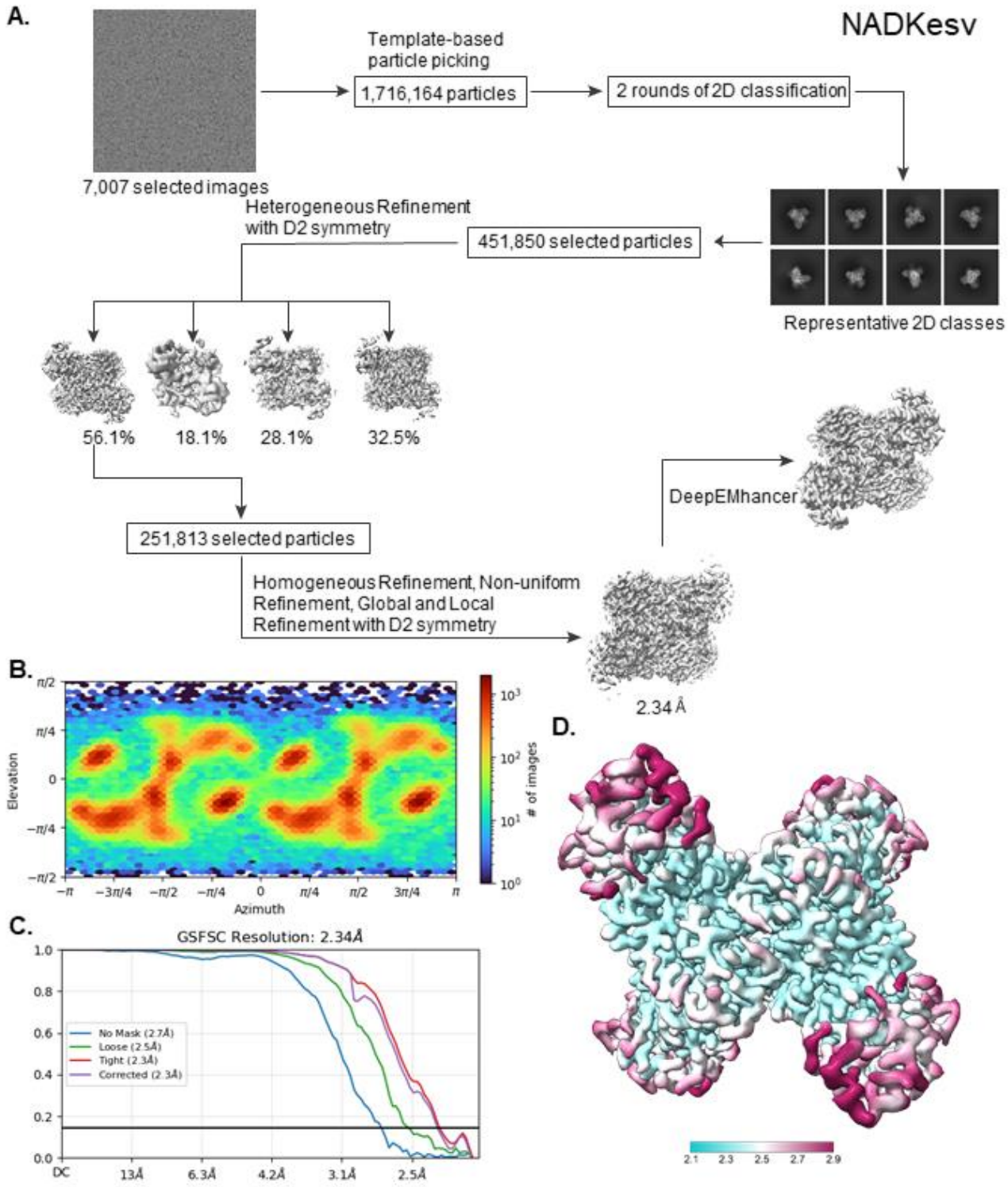
A.
NADKesv
Template-based particle picking
1,716,164 particles
2 rounds of 2D classification
7,007 selected images
Representative 2D classes
Heterogeneous Refinement with D2 symmetry
451,850 selected particles
56.1%
18.1%
28.1%
32.5%
DeepEMhancer
251,813 selected particles
Homogeneous Refinement, Non-uniform Refinement, Global and Local Refinement with D2 symmetry
2.34 Å
B.
Elevation
Azimuth
# of images
C.
GSFSC Resolution: 2.34Å
No Mask (2.7Å)
Loose (2.5Å)
Tight (2.3Å)
Corrected (2.3Å)
DC
13Å
6.3Å
4.2Å
3.1Å
2.5Å
D.
2.1
2.3
2.5
2.7
2.9

Figure S10: Cryo-EM Image Processing for $NADK_{esv}$.

(**A**) Flowchart of the cryo-EM data processing of $NADK_{esv}$.

(**B**) The Euler angle distribution plot from cryoSPARC.

(**C**) The gold-standard Fourier shell correlation (GS-FSC) curves from cryoSPARC.

(**D**) Local resolution estimation of the cryo-EM map of $NADK_{esv}$.

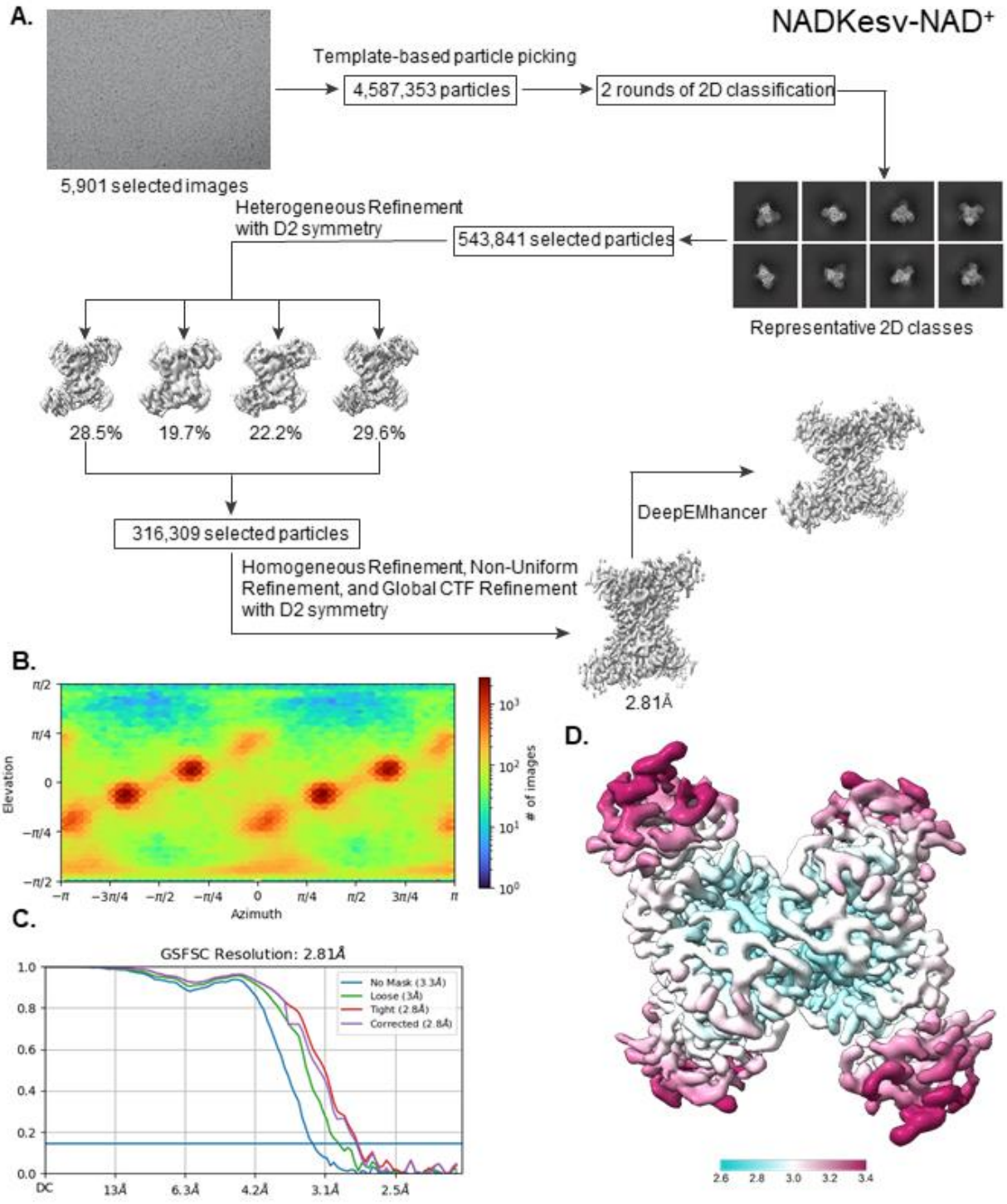
A.
NADKesv-NAD+
Template-based particle picking
4,587,353 particles
2 rounds of 2D classification
5,901 selected images
Representative 2D classes
Heterogeneous Refinement
with D2 symmetry
543,841 selected particles
28.5%
19.7%
22.2%
29.6%
316,309 selected particles
DeepEMhancer
Homogeneous Refinement, Non-Uniform
Refinement, and Global CTF Refinement
with D2 symmetry
2.81Å
B.
Elevation
Azimuth
# of images
C.
GSFSC Resolution: 2.81Å
No Mask (3.3Å)
Loose (3Å)
Tight (2.8Å)
Corrected (2.8Å)
D.

Figure S11: Cryo-EM Image Processing for $NADK_{esv}$-NAD^+.

(**A**) Flowchart of the cryo-EM data processing of $NADK_{esv}$ -NAD+.

(**B**) The Euler angle distribution plot from cryoSPARC.

(**C**) The gold-standard Fourier shell correlation (GS-FSC) curves from cryoSPARC.

(**D**) Local resolution estimation of the cryo-EM map of $NADK_{esv}$-NAD^+.